

Unveiling single-particle composition, size, shape, and mixing state of freshly emitted Icelandic dust via electron microscopy analysis

Agnesh Panta^{1,a}, Konrad Kandler¹, Kerstin Schepanski², Andres Alastuey³, Pavla Dagsson Waldhauserova^{4,5}, Sylvain Dupont⁶, Melanie Eknayan¹, Cristina González-Flórez^{7,b}, Adolfo González-Romero^{3,7}, Martina Klose⁸, Mara Montag¹, Xavier Querol³, Jesús Yus-Díez⁹, and Carlos Pérez García-Pando^{7,10}

¹Institute of Applied Geosciences, Technical University of Darmstadt, 64287 Darmstadt, Germany

²Department of Earth Sciences, Institute of Meteorology, Freie Universität Berlin, 12165 Berlin, Germany

³Institute of Environmental Assessment and Water Research (IDAEA-CSIC), 08034 Barcelona, Spain

⁴Faculty of Environmental and Forest Sciences, Agricultural University of Iceland, 311 Hvanneyri, Iceland

⁵Faculty of Environmental Sciences, Department of Water Resources and Environmental Modeling, Czech University of Life Sciences Prague, 165 00 Prague, Czech Republic

⁶INRAE, Bordeaux Sciences Agro, ISPA, Villenave d'Ornon, France

⁷Barcelona Supercomputing Center, 08034 Barcelona, Spain

⁸Department Troposphere Research, Institute of Meteorology and Climate Research (IMK-TRO), Karlsruhe Institute of Technology (KIT), Karlsruhe, Germany

⁹Center for Atmospheric Research, University of Nova Gorica, Vipavska 11c, SI-5270 Ajdovščina, Slovenia

¹⁰ICREA, Catalan Institution for Research and Advanced Studies, 08010 Barcelona, Spain

^anow at: Palas GmbH, 76187 Karlsruhe, Germany

^bnow at: Danish Meteorological Institute (DMI), 2100 Copenhagen, Denmark

Correspondence: Konrad Kandler (kandler@geo.tu-darmstadt.de)

1 Abstract.

2 Iceland is a significant high-latitude dust source area. Airborne Icelandic dust influences the climate system by interacting
3 with radiation, clouds, and biogeochemical cycles; it also affects snow and ice albedo and air quality. These impacts are sen-
4 sitive to the dust's mineralogical, chemical, and physical properties. However, comprehensive measurements and analyses of
5 Icelandic dust particles remain limited. This study examines dust samples collected during a field campaign in the Dyngju-
6 sandur desert (August-September 2021) using active and passive aerosol sampling. Over 190,000 individual particles, ranging
7 from 0.1 to 120 μm , were analyzed for their chemical and physical properties using scanning electron microscopy/energy
8 dispersive X-ray spectroscopy (ccSEM/EDX). Results show heterogeneity in particle size, shape, and composition. The most
9 abundant particle type was Medium-Al mixed particles, likely glass-like, comprising 35–92 % of the aerosol volume. Sulfate
10 particles, suggesting volcanic contributions, were detected in some samples. Iron (Fe) and titanium (Ti)-rich particles made
11 up 3.3 % and 6 % of the aerosol volume, respectively, mainly in the size fraction $<1 \mu\text{m}$. The median aspect ratio ranged
12 from 1.37 to 1.53, increasing with particle size. Our findings highlight key differences in Icelandic dust compared to Saharan
13 dust, including higher iron and titanium content and a lack of potassium in Icelandic dust. Additionally, Icelandic dust shows
14 a size-dependent increase in aspect ratio, unlike Saharan dust, which remains constant. These observations can improve model
15 simulations that account for the effect of high-latitude dust in the Earth System.

17 Mineral dust is one of the most important and prominent aerosol types. Dust impacts the Earth system via interactions with
18 radiation (Kok et al., 2023), clouds (Shi et al., 2022), atmospheric chemistry (Gaston, 2020), the cryosphere (Dong et al.,
19 2020) and ocean biogeochemistry (Hamilton et al., 2022). The chemical and mineralogical composition, morphology, and size
20 distribution of dust are critical parameters in determining its impact on the atmosphere and environment (Formenti et al., 2011;
21 Mahowald et al., 2014): the elemental composition determines the biogeochemical cycling of minerals (Shi et al., 2012), and
22 the material properties determine the optical properties, in particular with respect to light absorption (Sokolik et al., 1998).
23 Moreover, the distribution of the compounds in and among the particles (i.e., internal or external mixing) is another important
24 factor to consider. For example, the optical properties of aerosols, such as light absorption and scattering, are strongly dependent
25 on their mixing state (Lindqvist et al., 2014; Nousiainen and Kandler, 2015). In addition, chemical transformation processes,
26 such as heterogeneous reactions and secondary aerosol formation, are also considerably affected by whether particles are
27 internally or externally mixed (Ito and Feng, 2010). The mixing state can vary substantially depending on the regional aerosol
28 regime and emission sources, reflecting the diverse and heterogeneous nature of ambient particulate matter (Li et al., 2016).
29 Understanding these mixing structures is essential for assessing aerosol impacts on climate and air quality.

30 Although hot subtropical deserts are the largest contributors to the global dust cycle (Kok et al., 2021), recent research has
31 identified cold deserts at high latitudes as an important yet neglected dust source (Prospero et al., 2012; Bullard et al., 2016;
32 Meinander et al., 2022). High-latitude dust (HLD) regions are defined as north of $\geq 50^\circ\text{N}$ and south of $\geq 40^\circ\text{S}$ and include the
33 Arctic as a sub-region $\geq 60^\circ\text{N}$ (Meinander et al., 2022). Model simulations indicate that HLD sources contribute an estimated
34 1-5 % of global dust emission (Bullard et al., 2016; Groot Zwaafink et al., 2016; Meinander et al., 2022), while their impact
35 might be much higher due to their presence in an otherwise pristine, but sensitive environment (Schmale et al., 2021). Some
36 studies suggest that HLD sources may become more active in the future as glaciers retreat and expose new sediments (Bullard
37 et al., 2016; Meinander et al., 2022). While factors such as changes in precipitation and vegetation cover could counteract this
38 effect by stabilizing dust source areas (Aryal and Evans, 2023), field observations from Iceland demonstrate that precipitation
39 has limited influence on dust suspension from glacial outwash plains. Dust storms have been observed during high precipitation
40 periods and even with low winds, with dust plumes occurring within hours after rainfall (Waldhauserova et al., 2014). Further
41 work is needed to understand the net effect on HLD emissions due to climate change.

42 In the northern hemisphere, Iceland is a major high-latitude source of dust (Arnalds et al., 2001, 2016). While Iceland
43 as a whole is humid from a climatological point of view, some regions in the interior are semi-arid due to shielding by the
44 surrounding mountains (Arnalds et al., 2016). Therefore, it is one of the most active aeolian areas on Earth, consisting of sandy
45 deserts, which undergoes intensive aeolian processes (Arnalds et al., 2001, 2016). Glaciers cover about 11 % of Iceland's land
46 surface (Björnsson and Pálsson, 2008). Glacier activity results in the production of glacial sediment of which in particular the
47 fine fraction is transported by glacial meltwater. After drying, these fine sediments are prone to wind erosion (Bullard et al.,
48 2016) and frequently emit dust (Arnalds, 2010; Arnalds et al., 2016). The sandy areas of Iceland have dark surfaces consisting
49 of mostly basaltic volcanic glass (Arnalds et al., 2001). Hence, due to the different geological origin and a different weathering

regime compared to lower latitudes with a different climate, the properties of Icelandic dust are significantly different compared to northern African and Asian dust (Baldo et al., 2020, 2023; González-Romero et al., 2024b).

Icelandic dust serves as ice-nucleating particles across the North Atlantic and Arctic (Paramonov et al., 2018; Sanchez-Marroquin et al., 2020; Kawai et al., 2023). However, the abundance, sources, and nature of INPs in the high latitudes remain poorly understood (Murray et al., 2021; Xi et al., 2022). Furthermore, Icelandic dust can be strongly light-absorbing due to the presence of magnetite-like particles (Yoshida et al., 2016). In addition, it has different shapes, lower densities, higher porosity, increased roughness, and darker colors compared to other desert dusts (Butwin et al., 2020; Richards-Thomas et al., 2021). Icelandic dust provides a large surface for heterogeneous reactions with SO₂ uptake, thus providing a major sink of sulfur in volcanic clouds (Urupina et al., 2019; Lasne et al., 2022). Icelandic dust also has a strong influence on the mass balance of glaciers in Iceland (Wittmann et al., 2017) and thereby have a stronger positive direct radiative forcing on climate (Baldo et al., 2023), as indicated by its optical properties alone. Emitted Icelandic dust can be transported towards the North Atlantic Ocean (Dagsson-Waldhauserova et al., 2013; Moroni et al., 2018) as well as to glaciers in Greenland (Meinander et al., 2016). The transported dust could also potentially influence marine biota within ecosystems in the Arctic Ocean (Dagsson-Waldhauserova et al., 2017).

Information on the physico-chemical differences across dust sources is essential for dust modeling and understanding its climate impact. The mineralogical composition of dust can differ greatly between regions because of geological and climatic influences (Claquin et al., 1999; Journet et al., 2014). However, many Earth models generally assume a globally uniform dust composition, due to the lack of comprehensive global data on the parent soil. Only a few models consider variations in dust mineralogy (Perlwitz et al., 2015; Gonçalves Ageitos et al., 2023; Song et al., 2024) by utilizing global soil type atlases and extrapolating from a small set of analyses. In situ studies, which could provide more accurate data, are often limited by several challenges. For one, source areas are difficult to study due to the remote and harsh nature of source regions, as well as the technical difficulties in sampling during high dust events. Instruments used for measuring dust in these conditions are often prone to saturation or damage, further complicating data collection. Moreover, the large size range, spanning from few microns to hundreds of microns, of mineral dust particles adds another layer of complexity. Field measurements often struggle to capture the larger supermicron particles, which constitute a significant fraction of the total mass. Additionally, different sampling methods based on properties such as optical, inertial, or electrical characteristics often yield data that are difficult to compare, as these methods depend on particle composition, size, and shape. Without parallel measurements of physico-chemical properties, the data from different techniques can be difficult to reconcile (Hinds, 1999). These issues underscore the need for more robust, in situ studies that can provide high-resolution data on particle composition, size distribution, and source characterization to improve the accuracy of dust-climate interaction models.

To tackle these and other knowledge gaps, we performed a large-scale field experiment in the most prolific dust source region of Iceland, the desert of Dyngjunsandur, in August and September 2021. The campaign was co-organized by two projects: FRontiers in dust minerAloGical coMposition and its Effects upoN climaTe (FRAGMENT) and Iceland as a model for high-latitude dust sources – a combined experimental and modeling approach for characterization of dust emission and transport processes (HiLDA). The goal of the campaign was to improve our fundamental understanding of the emitted dust

size distribution and size-resolved mineralogical composition along with their relationship with the parent soil properties and meteorology. The campaign included detailed study of the mineralogical composition, particle size distribution, mode of occurrence of Fe, degree of cohesion, and visible–near infrared (VNIR) reflectance spectra of the dust-emitting sediment (González-Romero et al., 2024b). Additionally, the study focused on the small scale meteorology and size-resolved fluxes (Dupont et al., 2024). This campaign followed another one performed in Morocco (2019) (Panta et al., 2023; González-Flórez et al., 2023; González-Romero et al., 2023) and preceded two other campaigns in the US (2022) (González-Romero et al., 2024a) and Jordan (2022) (Dupont et al., 2024), all them performed within the FRAGMENT project.

This study focuses on the analysis of composition, size, and shape of the freshly emitted dust using electron microscopy. Computer controlled scanning electron microscopy coupled with energy-dispersive X-ray analysis (ccSEM/EDX) enables the investigation of the elemental and morphological composition of a large number of aerosol particles leading to higher counting statistics that are representative of the major particle-type present in the collected sample (Kandler et al., 2007; Scheuven et al., 2011; Kandler et al., 2020; Panta et al., 2023). We focus on the composition of airborne-sampled freshly emitted mineral dust close to the source as well as in the outflow regions, the average shape parameter (aspect ratio) and its relationship with size and composition, the difference in composition during different dust episodes as well as the iron contribution to the single particles. We conclude the paper by comparing high-latitude Icelandic dust and mid-latitude Moroccan dust that were sampled using the same collection technique and analysed using ccSEM/EDX (Panta et al., 2023).

2 Experimental methods

2.1 Study area and sampling sites

The intensive campaign was carried out in the highlands of Iceland for a period of 6 weeks during August-September 2021. During these weeks, measurements were carried out in Dyngjúsandur (DYS) as well as the outflow region (MRS, SRS, HRS, and VFS) as shown in Fig.1. The coordinates of all the sampling sites are given in Table S1 in the Supplement. Dyngjúsandur lies north of Vatnajökull glacier in the interior of Northeast Iceland and is characterized by various surface pathways of aeolian sediments. It has a dry, cold climate with an annual precipitation of less than 400 mm and is known to be one of the most extensive dust source areas in Iceland with frequent dust events observed during summer (Arnalds et al., 2016). During the campaign, temperatures ranged mostly between 5 °C and 15 °C. There were only six days when temperatures exceeded 15 °C, with the highest 15-minute average peak at 2m height recorded as 21.61 °C on August 24th, breaking the previous maximum temperature record for August. This temperature rise caused the Vatnajökull glacier to experience intensified daily meltwater discharge, leading to complete flooding of the measurement site. The increased wind speed during the following days, with average values exceeding 18 ms⁻¹ at 9.9 m height and gusts above 25 ms⁻¹, resulted in intense dust storms that lasted throughout the day. This was a significant change from the initial period of the campaign, which had weaker winds, more frequent precipitation, and shorter and less intense dust events (Dupont et al., 2024; González-Romero et al., 2024b).

The main site (DYS) was located in a terminal lake connected to a nearby glacier (N 64° 54' 55", W 16° 46' 35", 710 m a.s.l.; see Fig. 1). The area is topographically mostly flat and is devoid of vegetation or other obstacles. It has however melt

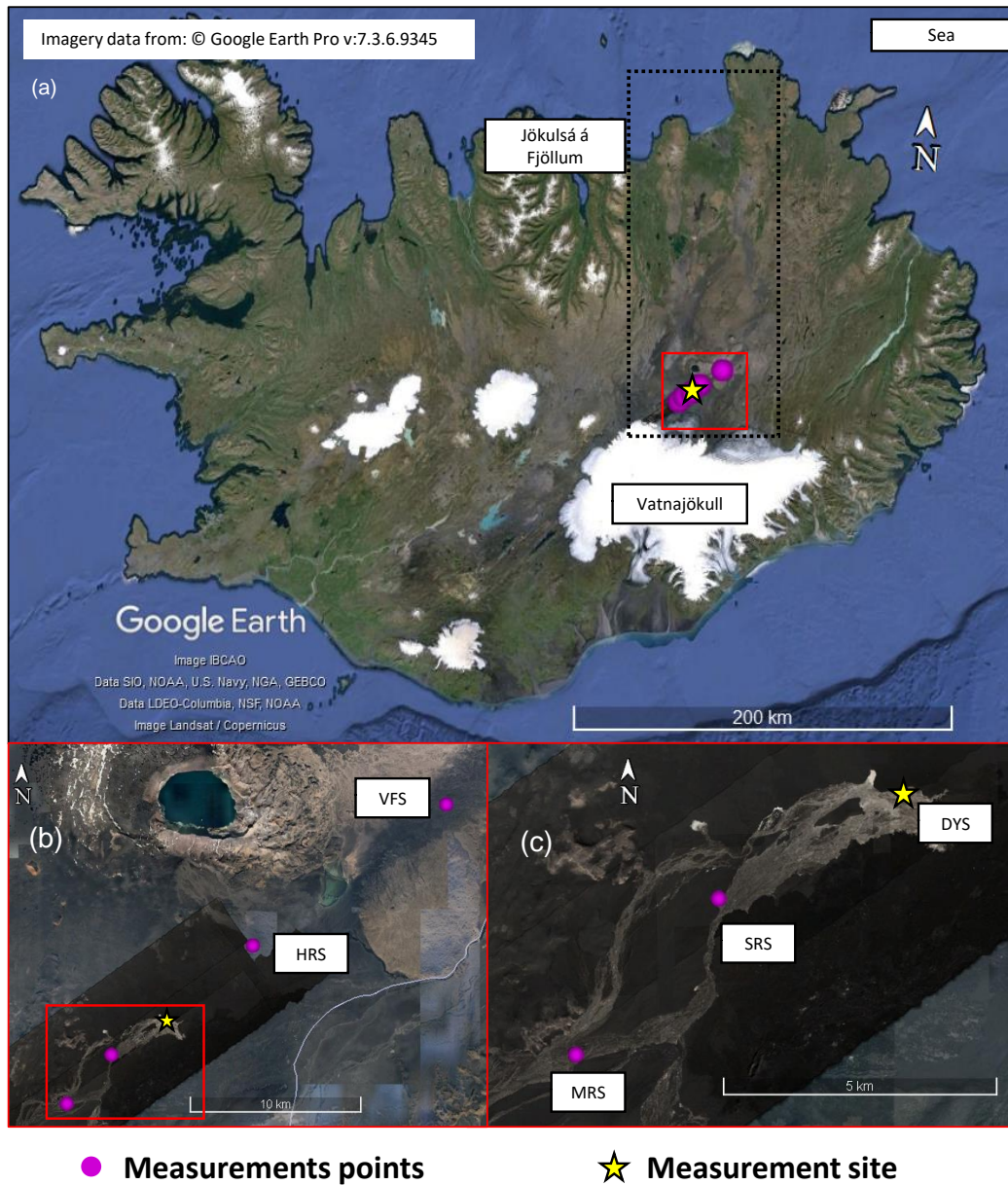


Figure 1. (a) Basemap of Iceland showing the hotspot region of Jökulsá á Fjöllum with dotted points. The yellow star indicates the main experimental site "DYS", and the purple dots mark the locations of deposition samplers in the outflow regions. (b) Zoom-in of the hotspot region showing the samplers "HRS" and "VFS" located northeast of the main site. (c) Zoom-in showing the samplers "SRS" and "MRS" located southwest of the main site.

118 water channels due to the glacier discharge causing glacio-fluvial sediment to be frequently replenished with finer particles on
119 top, that are prone to dust emission under favourable conditions (González-Romero et al., 2024b; Dupont et al., 2024). The
120 main site (DYS) was heavily instrumented with several ground-based monitoring devices for meteorological and airborne dust
121 measurements. In addition to the main measurement site, dust deposition samplers were deployed throughout the region to
122 study the spatial distribution and composition of dust. These auxiliary sites are labeled MRS, SRS, HRS, and VFS (see Fig. 1).
123 MRS and SRS are located near DYS, while HRS and VFS are positioned further downwind, with VFS situated on a hilltop.
124 MRS, SRS, and HRS have surface characteristics similar to the main site and are part of the Jökulsá á Fjöllum river basin. VFS
125 is located approximately 60 meters above the riverbed and is well-positioned to monitor airborne dust leaving the riverbed
126 source.

127 **2.2 Particle sampling**

128 Particles were collected using flat-plate samplers (FPS) and free-wing impactors (FWI) both of which are briefly described in
129 the section below. A detailed description and methodology of sampling techniques have been described in previous publications
130 (Kandler et al., 2018; Panta et al., 2023). All samples have been collected on top of pure carbon adhesive substrates (Spectro
131 Tabs, Plano GmbH, Wetzlar, Germany) mounted to standard scanning electron microscopy (SEM) aluminum stubs. Pure carbon
132 substrate was chosen because of the low-Z background providing a contrast between particles and background as well as the
133 different elemental composition of the background and the substances of interest. All adhesive samples were stored in standard
134 SEM storage boxes (Ted Pella Inc., Redding, CA, USA) in dry conditions. FWI samples were collected twice per day with a
135 typical sampling duration of a few minutes to an hour whereas the exposure time was 8–48 h for the FPS. The sample substrate
136 exposure time was dependent on the estimated aerosol concentrations in order to have a statistically significant number of
137 particles on the substrate for individual particle analysis.

138 The differences in sampling durations reflect the distinct operational modes of the samplers. Passive samplers (i.e. FPS),
139 require longer integration times (8–48 h) to accumulate sufficient aerosol loading due to their low collection velocities. In
140 contrast, active samplers (i.e. FWI) can operate over much shorter time frames (minutes to 1 h), as their high effective deposition
141 velocities ensure adequate particle loading. Matching the durations across all systems would either result in under-loading of
142 the passive samples or overloading of active ones. Examples of low-magnification electron micrographs of dust collected by
143 the flat-plate deposition sampler are shown in section S7 of the supplement, providing an overview of the diversity of the dust
144 grains.

145 **2.2.1 Free-wing Impactor (FWI)**

146 A free-rotating wing impactor (Kandler et al., 2018; Panta et al., 2023) was used to collect particles larger than approximately
147 3 μm (projected diameter). The FWI has a carbon adhesive impaction surface on the aluminum stub attached to a rotating arm
148 that moves through the air; particles deposit on the moving plate due to their inertia. The rotating arm is moved at a constant
149 speed by a stepper motor, which is fixed on a wind vane, aligning the FWI to the wind direction. The substrate itself is oriented
150 perpendicular to the air stream vector (resulting from wind and rotation speeds) which is maintained by a small wind vane

151 attached to the rotating arm. The particle size cutoff is defined by the impaction parameter, i.e., by rotation speed, wind speed,
 152 and sample substrate geometry. Table 1 gives an overview of the FWI sampling times. The reported time is in UTC, which is
 153 also local time for Iceland.

Table 1. Sampling times for free-wing impactor samplers at DYS

ID	Start date & time	End date & time	Exposure time (min)	ID	Start date & time	End date & time	Exposure time (min)
1	09.08.2021 15:45	09.08.2021 17:45	120	22	23.08.2021 16:04	23.08.2021 16:08	4
2	10.08.2021 12:35	10.08.2021 14:35	120	23	23.08.2021 16:15	23.08.2021 16:16	1
3	10.08.2021 17:43	10.08.2021 17:57	14	24	31.08.2021 19:06	31.08.2021 19:07	1
4	10.08.2021 18:04	10.08.2021 18:07	3	25	01.09.2021 19:08	01.09.2021 19:09	1
5	11.08.2021 15:08	11.08.2021 15:18	10	26	01.09.2021 19:14	01.09.2021 19:16	2
6	11.08.2021 15:24	11.08.2021 15:39	15	27	02.09.2021 10:15	02.09.2021 10:45	30
7	12.08.2021 17:23	12.08.2021 17:38	15	28	02.09.2021 19:00	02.09.2021 19:30	30
8	14.08.2021 16:08	14.08.2021 17:10	62	29	03.09.2021 09:30	03.09.2021 10:30	60
9	15.08.2021 16:29	15.08.2021 16:30	1	30	03.09.2021 11:27	03.09.2021 11:34	7
10	15.08.2021 16:33	15.08.2021 16:36	3	31	03.09.2021 11:38	03.09.2021 11:47	9
11	15.08.2021 16:41	15.08.2021 16:46	5	32	03.09.2021 19:10	03.09.2021 19:15	5
12	16.08.2021 18:20	16.08.2021 18:21	1	33	04.09.2021 09:25	04.09.2021 09:30	5
13	16.08.2021 18:23	16.08.2021 18:26	3	34	04.09.2021 09:33	04.09.2021 09:38	5
14	16.08.2021 18:27	16.08.2021 18:32	5	35	04.09.2021 09:45	04.09.2021 10:00	15
15	17.08.2021 18:41	17.08.2021 18:44	3	36	04.09.2021 18:40	04.09.2021 18:41	1
16	17.08.2021 18:45	17.08.2021 18:50	5	37	04.09.2021 18:43	04.09.2021 18:45	2
17	19.08.2021 16:40	19.08.2021 17:10	30	38	05.09.2021 09:35	05.09.2021 09:37	2
18	20.08.2021 15:48	20.08.2021 17:48	120	39	05.09.2021 09:38	05.09.2021 09:38	0.5
19	21.08.2021 13:22	21.08.2021 13:52	30	40	05.09.2021 20:06	05.09.2021 20:16	10
20	22.08.2021 17:02	22.08.2021 17:04	2	41	05.09.2021 20:20	05.09.2021 20:22	2
21	22.08.2021 17:10	22.08.2021 17:11	1				

154 **2.2.2 Flat plate sampler**

155 The flat-plate dry deposition sampler (FPS) used in this work is similar to the original FPS used in Ott and Peters (2008),
 156 except for a retraction of the deposition surface to the level of the lower plate (Waza et al., 2019). It consists of two round
 157 brass plates (top-plate diameter of 203 mm, bottom plate 127 mm, thickness 1 mm each) mounted 16 mm apart. The plates
 158 protect the substrate from precipitation and reduce the effects of wind speed by reducing the smallest turbulence to the distance
 159 between the parallel plates. This design prevents larger droplets (> 1 mm) from reaching the surface of the SEM stub at low
 160 wind speeds (Ott and Peters, 2008). The main triggers for particle deposition on the substrate are diffusion, settling by gravity,
 161 and turbulent inertial forces.

162 A total of 29 sample substrates for electron microscopy were analysed. There were a few samples that could not be analysed
 163 because of overloading of the substrate. Table 2 gives an overview of the sampling times. The reported time is in UTC, which
 164 is also local time for Iceland. The sampling time for samples collected at surrounding locations is given in the Supplement
 165 Table S2-S5.

Table 2. Sampling times for flat-plate samplers at Dyngjusandur (DYS)

ID	Start date & time	End date & time	Exposure time (min)	ID	Start date & time	End date & time	Exposure time (min)
1	09.08.2021 12:00	10.08.2021 16:15	1695	16	31.08.2021 08:45	31.08.2021 10:05	80
2	10.08.2021 16:20	11.08.2021 14:30	1330	17	31.08.2021 10:05	31.08.2021 10:45	40
3	11.08.2021 14:40	12.08.2021 17:50	1630	18	31.08.2021 10:45	31.08.2021 18:30	465
4	12.08.2021 18:00	13.08.2021 18:00	1440	19	31.08.2021 18:40	01.09.2021 09:05	865
5	13.08.2021 18:05	14.08.2021 18:00	1435	20	01.09.2021 09:15	01.09.2021 10:40	85
6	14.08.2021 18:05	15.08.2021 18:23	1458	21	01.09.2021 11:55	01.09.2021 18:15	380
7	15.08.2021 18:25	16.08.2021 18:39	1454	22	01.09.2021 18:30	02.09.2021 18:35	1445
8	16.08.2021 18:34	17.08.2021 19:00	1466	23	02.09.2021 18:35	03.09.2021 19:20	1485
9	17.08.2021 19:00	19.08.2021 17:08	2768	24	03.09.2021 19:20	04.09.2021 18:35	1395
10	19.08.2021 17:10	21.08.2021 16:50	2860	25	04.09.2021 18:35	04.09.2021 19:40	65
11	21.08.2021 16:50	22.08.2021 17:35	1485	26	04.09.2021 19:45	05.09.2021 09:35	830
12	22.08.2021 20:00	23.08.2021 18:05	1325	27	05.09.2021 09:35	05.09.2021 10:30	55
13	23.08.2021 18:10	25.08.2021 10:00	2390	28	05.09.2021 10:30	05.09.2021 20:30	600
14	30.08.2021 19:12	31.08.2021 08:20	788	29	05.09.2021 20:30	07.09.2021 10:45	2295
15	31.08.2021 08:25	31.08.2021 08:35	10				

2.3 Scanning electron microscopy (SEM)

2.3.1 Composition

The elemental composition and morphology of individual particles were analyzed using computer-controlled scanning electron microscopy (ccSEM; FEI ESEM Quanta 400 FEG, Eindhoven, The Netherlands) coupled with energy dispersive X-ray spectroscopy (EDX; EDAX Phoenix, EDAX, Tilburg, The Netherlands and Oxford X-Max 150, Oxford Instruments, Abingdon, United Kingdom). The samples were examined in the high vacuum mode of the instrument ($\sim 5 \times 10^{-6}$ Pa chamber pressure) without any pre-treatment. Prior to automated analysis, samples were checked for possible surface defects and particle coverage patterns. Areas with surface defects (for example, bubbles in the substrate) and overloaded samples were excluded from further data processing. Sample analysis was automated by the software-controlled electron microscope (Oxford Aztec 4.4). Automated particle segmentation from the background was performed based on the backscatter electron signal. An acceleration voltage of 12.5 kV, beam current of 18 nA, spot size 5 (beam diameter ~ 3 nm) and a working distance of approximately 10 mm were used to produce the optimum number of input counts in the EDX detector. Scanning resolution was tuned to particle size. For the FPS, 160 nm per pixel were used to identify particles up to 0.5 μm (equivalent projected area diameter) and for the FWI, 360 nm per pixel was used to identify the largest particles (mainly particles larger than 2.5 μm). The X-ray signal was collected for each particle for a duration of 15 to 20 seconds (EDAX) and 2 seconds (Oxford), resulting in a total of 40,000 to 100,000 counts. During this time, the beam scanned over the particle's cross-sectional area. Chemistry information is derived by EDX. The internal ZAF correction (Z – atomic number, A – absorption, F – fluorescence, accounting for material-dependent efficiencies) of the detector/software system – based on inter-peak background radiation absorption measurements for correction – was used for obtaining quantitative results.

185 In numerous places in the present work, relative elemental concentrations and ratios thereof are reported by the correspond-
186 ing element symbols. These concentrations always refer to atom % (and not weight %).

187 2.3.2 Aspect Ratio

188 The two-dimensional (2D) shape of individual dust particles is presented here as aspect ratio (AR) and was calculated by the
189 image analysis integrated into the SEM-EDX software AZtec. AZtec software manual defines AR as the ratio of the major to
190 the minor axis of the elliptical fit on the projected particle area, such that features with shapes similar to spheres have an AR
191 that is approximately 1, whereas ovals or needles have an AR that is greater than 1. A caveat of 2-D imaging is that it can yield
192 different shapes of 3-D particles depending on their orientation on the sampling substrate (Huang et al., 2020).

193 2.3.3 Projected-area and volume-equivalent diameters

194 In this study, the image analysis integrated into the SEM-EDX software AZtec is used to determine the size of particles in terms
195 of projected area diameter. Projected area diameter (d_p) is the diameter of a circle having the same area as the dust particle
196 projected in a two-dimensional image and is calculated as:

$$197 \quad d_p = \sqrt{\frac{4 \cdot A}{\pi}}, \quad (1)$$

198 in which A is the area covered by the particle on the sample substrate.

199 Following Ott and Peters (2008), the volume-equivalent diameter (sphere with the same volume as an irregular shaped
200 particle) also called the geometric diameter (d_v) is estimated from the projected area diameter via a volumetric shape factor
201 expressed by particle projected area and perimeter (P) as follows:

$$202 \quad d_v = \frac{4\pi A}{P^2} d_p = \frac{1}{P^2} \sqrt{64\pi A^3}. \quad (2)$$

203 In the literature there are several definitions for “fine”, “coarse”, “super-coarse” and “giant” aerosol particles. In this paper
204 we use the size terminology defined in terms of volume-equivalent (geometric) diameter (D) as described in Adebiyi et al.
205 (2023) for fine dust ($D < 2.5 \mu\text{m}$), coarse dust ($2.5 \leq D < 10 \mu\text{m}$), super-coarse dust ($10 \leq D < 62.5 \mu\text{m}$), and giant dust
206 ($D > 62.5 \mu\text{m}$). Furthermore, all particle diameters presented here are converted from projected area-equivalent diameter to
207 volume-equivalent (geometric) diameter (unless stated otherwise). The reason for this conversion is that geometric diameter is
208 used in global aerosol models to quantify dust size (Mahowald et al., 2014).

209 Particle volume was then computed as

$$210 \quad V = \frac{\pi}{6} \cdot d_v^3. \quad (3)$$

211 2.4 Mineral identification

212 The mineralogical identification in this study is based on the elemental composition of each individual particle. Previous
213 studies have used SEM–EDX analysis to semi-quantitatively identify the mineralogical composition of individual dust particles
214 (Kandler et al., 2007; Scheuvens et al., 2011; Kandler et al., 2020; Panta et al., 2023). As SEM–EDX detects the elemental
215 composition of particles, this alone is not enough to accurately identify their mineral phase. However, since the elemental
216 composition of many common minerals is known, the elemental ratio provided by EDX can be used as an approach to the
217 mineralogical identification of the aerosol particles, as long as each particle is assumed to be composed of a single mineral type.
218 There are some minerals (e.g., quartz, sea-salt) that can be identified more reliably, while others are generally indistinguishable
219 (e.g., Gypsum/anhydrite, hematite/magnetite), and some which may contain ambiguous compositions and therefore are prone
220 to a potential classification error (e.g., micas, smectites) using SEM–EDX. Additionally, although individual particles are
221 typically chosen for EDX analysis, some mixtures may be present and could lead to discrepancies between EDX results and
222 the true mineral composition.

223 Based on the single particle composition quantification, an elemental index ($|X|$) for the element X is defined as the atomic
224 ratio of the concentration of the element considered and the sum of the concentrations of the element quantified (Kandler et al.,
225 2007, 2018),

$$226 \quad |X| = \frac{X}{Na + Mg + Al + Si + P + S + Cl + K + Ca + Ti + Cr + Mn + Fe}, \quad (4)$$

227 where the element symbols represent the relative contribution in atom % measured for each particle. The chemical com-
228 position of each particle, including the major elements F, Na, Mg, Al, Si, P, S, Cl, K, Ca, Ti, V, Cr, Mn, Fe, Zn, and Pb,
229 was determined using EDX and is reported as normalized atomic percentages. Since the substrate is composed of carbon, the
230 element C was excluded from the quantification. N and O were disregarded as well due to their high measurement error.

231 3 Results

232 3.1 Particle-type characterization and their relative abundances

233 Chemical compositions of more than 128,000 particles were measured from the samples collected at Dyngjúsandur. Addition-
234 ally 62,400 particles were analysed from surrounding locations. Based on the chemical composition derived from EDX, the
235 particles were classified into different particle groups. The full classification can be found in section S3 in supplement.

236 The classification scheme is primarily based on our previous work (Kandler et al., 2007, 2018; Panta et al., 2023). However,
237 as the geology of Iceland is different to that of low- and mid-latitude dust sources, other mineralogical particle groups are
238 required and, therefore, new boundary conditions were developed. Dyngjúsandur is mainly characterised by basaltic volcanic
239 glasses formed below Vatnajökull glacier during subglacial eruptions with pyroxene, olivine and plagioclase as other significant
240 phases (Baratoux et al., 2011). Dust resuspension of surface sediment samples from five major Icelandic dust hotspots including

241 Dyngjusandur also showed amorphous basaltic materials to be dominant with around 70 wt % observed for the Dyngjusandur
 242 sample (Baldo et al., 2020). In the following, the major particle groups found are described.

243 **3.1.1 Medium Al mixed silicates**

244 The most frequent particles in Dyngjusandur are classified as Medium Al mixed silicates (MAS) based on our elemental
 245 classification scheme. The name is chosen to be generic and descriptive, as they most probably do not represent a mineral, but
 246 instead a glassy substance. Figure 2 presents the size-resolved average elemental composition and a 2D histogram of MAS
 247 particles. It is characterized by the presence of elements such as Si, Al, Fe, Ca, Mg, and Na in EDX spectra with Al/Si of 0.34
 248 ± 0.04 (mean \pm standard deviation), Ca/Si of 0.21 ± 0.05 , Mg/Si of 0.17 ± 0.05 . The Fe/Si ratio is slightly higher in fine
 249 mode (0.28 ± 0.07) and decreases in coarse (0.22 ± 0.05) and super-coarse (0.20 ± 0.05) mode. In addition, Si, Al, Ca, and
 250 Mg exhibit consistent trends across size range, whereas Fe decreases and Na increases as size increases.

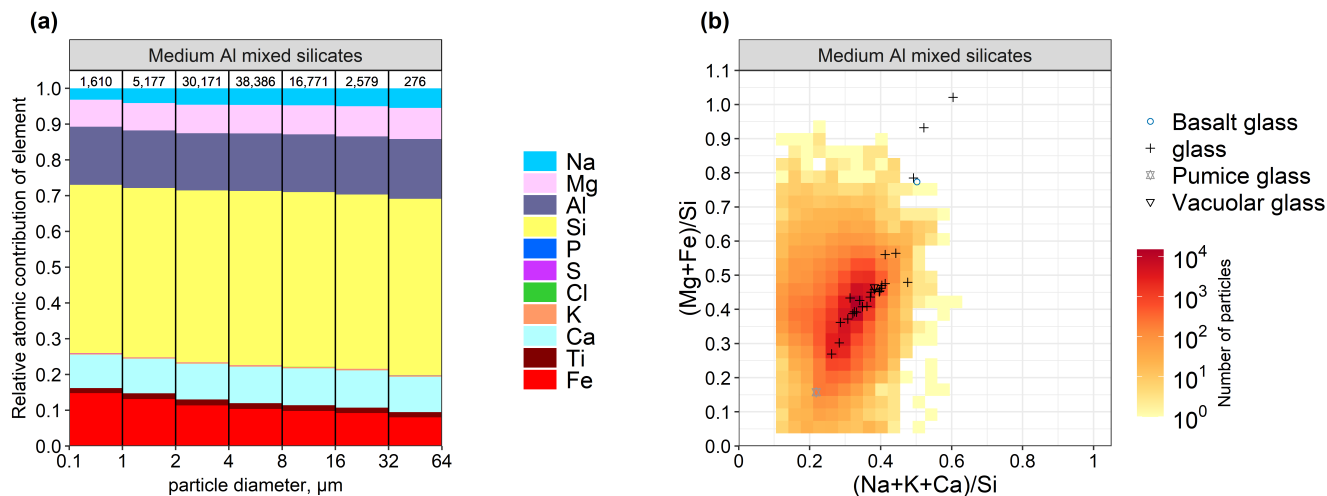


Figure 2. (a) Average elemental composition (atomic fraction) as a function of particle size for the Medium Al mixed silicates (MAS) particles at Dyngjusandur from deposition plate and free-wing impactor samples. The numbers on top represent total particle counts in the given size bin. (b) Two-dimensional histogram with respect to element atomic concentration ratios for MAS particles. In addition, positions and classifications of particles identified manually by composition and morphology are shown.

251 As using chemistry alone is not sufficient to classify particles into glass, additional analysis was performed. A select number
 252 of particles was manually analyzed using SEM and classified as glass. Figure 2b shows the derived elemental ratios for these
 253 glass particles (each dot representing one particle) together with the two dimensional histogram for the particles classified
 254 as MAS using ccSEM. For illustration, images and elemental mappings of the MAS particles are given in the electronic
 255 supplement (section S8 and S9). The glassy structure becomes nicely visible by the river line fractures and the smooth surfaces.
 256 In some cases, a pumice structure is recognizable. While small variations in composition are detected, in general this group is
 257 homogeneous with respect to composition.

258 Furthermore, X-ray diffraction (XRD) analysis was performed on the surface sediments (González-Romero et al., 2024b).
259 The XRD analysis revealed that a significant component (79 ± 11 wt%) of the sediment consists of an amorphous phase,
260 most probably volcanic glass and its nano-sized weathering product (hydrated amorphous Si-bearing). This observation aligns
261 with the anticipated composition, given the predominantly basaltic nature of the magmas coming from the Grímsvötn volcanic
262 systems, which serve as the primary source for the Dyngjúsandur dust hotspot (Vogel et al., 2017).

263 Considering the XRD analysis results, which indicate the presence of amorphous basaltic material (volcanic glass) in the
264 Icelandic sediments, it can be inferred that the particles classified as MAS are likely to be glassy particles based on the elemental
265 ratios derived from the manual SEM analysis and the composition of the parent sediment.

266 3.1.2 Pyroxene/amphibole-like

267 Pyroxenes are rock-forming inosilicate minerals and have the general formula $XY(\text{Si},\text{Al})_2\text{O}_6$, where X and Y are most com-
268 monly sodium, magnesium, calcium, or iron. Pyroxene minerals usually have volcanic origin and are typically not present
269 in low latitude mineral dust. Previous studies have reported pyroxene (augite) to be the dominant mineral phases present in
270 Dyngjúsandur (Baratoux et al., 2011; Baldo et al., 2020). These particles can potentially act as ice nucleating particle as recent
271 work with volcanic tephra samples (volcanic ash) indicates that some pyroxene phases can onset freezing at temperatures near
272 -10 °C (Maters et al., 2019).

273 3.1.3 Interm.-Plag.-like

274 The Interm.-Plag.-like class consists of particles whose compositions fall between those of pyroxene and plagioclase. This
275 intermediate composition reflects a balance between calcium and sodium. Like pyroxene, plagioclase minerals are of volcanic
276 origin and are typically absent in mineral dust from low-latitude regions. Studies of sediment mineralogy as well as mineral
277 dust from Dyngjúsandur have identified the presence of plagioclase (González-Romero et al., 2024b; Moroni et al., 2018;
278 Baratoux et al., 2011).

279 3.1.4 Silicate mixtures

280 The groups "Other silicates", "Complex silicate (high Al)" and "Complex silicate (moderate Al-low alkali)" show no matches
281 with the common mineral phases. Nevertheless, they form distinct point clusters. This indicates that they have a specific chem-
282 ical composition depending on the group, but cannot be assigned to any mineral phase. Their position between compositions
283 of mineral phases indicates that the particles are structurally still in the process of fractionation from the igneous melt glass.

284 3.1.5 Iron-rich particles

285 Iron-rich particles were characterized by high relative fraction of Fe, with varying amount of mainly Si, Ca, and Ti present
286 and can be divided into two main categories: (a) Fe-oxide/Fe-hydroxide-like and (b) Titanomagnetite-like. These were also
287 observed in previous studies of surface sediment samples from Dyngjúsandur (Baldo et al., 2020). Hematite occurs mostly as a

secondary product of weathering in soils (Deer et al., 2013). As the sediments from Dyngjusandur show low degree of chemical weathering (Arnalds et al., 2016; Baldo et al., 2020), the Fe-oxide/Fe-hydroxide group are more likely to be magnetite-like than hematite-like. This was also observed in the sediment analysis of Dyngjusandur where the average bulk Fe content is 9.5 ± 0.4 wt% (González-Romero et al., 2024b). Furthermore, with increasing particle size in the Fe-oxide/Fe-hydroxide group, the contribution of Fe is slightly reduced and some elements mainly Ca is enhanced suggesting that these particles are increasingly internally mixed with other phases as particle size increases. The Titanomagnetite-like group is characterized with relatively high concentration of Ti in magnetite. Both of these particle types are observed mainly in diameters smaller than 4 μm and are generally mixtures of different minerals rather than pure component.

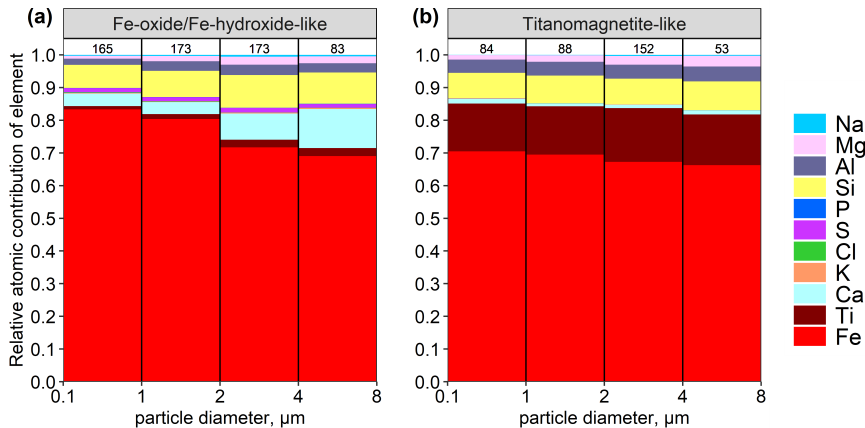


Figure 3. Average elemental composition as a function of particle size for (a) Fe-oxide/Fe-hydroxide-like and (b) Titanomagnetite-like. The legend shows element index for each respective element. The numbers on top represent total particle counts in the given size bin.

3.1.6 Sulfate

Sulfate aerosol particles are produced in the atmosphere through the oxidation of sulfur dioxide emitted by various sources. Volcanic emissions are the primary natural source of sulfur dioxide SO_2 (Carn et al., 2017), accounting for about 25 % of tropospheric sulfate aerosol burden (Lamotte et al., 2021). The emitted SO_2 undergoes oxidation in the atmosphere to form gaseous sulfuric acid, which then converts to sulfate aerosol particles. Furthermore, some mineral dust particles (e.g., calcite) can transform into other particle types through heterogeneous reactions with SO_2 (Li et al., 2014). The measurement period coincided with the basaltic eruption at Mt. Fagradalsfjall (March–September 2021) which released volcanic sulphur dioxide (SO_2) (Esse et al., 2023). Sulfate particles typically appeared to be spherical (see Figure S6 in the Supplement) although some extreme aspect ratios were also observed due to needle-like structure of these particles. Most of the sulfate observed falls into the group of Ammonium sulfate-like particles due to the lack of the common cations like Na, Mg, K or Ca, which is consistent with its formation by gas-to-particle conversion from the volcanic plume (Boulon et al., 2011).

307 **3.2 Relative abundances of various types of particles**

308 Figure 4 shows the relative volume abundance of the various particle types observed in the Dyngjúsandur samples. During
309 the measurement campaign, the composition of the aerosol particles in each sample did not exhibit a large sample-to-sample
310 variability except for few sulfate intrusion events (see Fig. S1 and S2 for individual samples collected on a deposition plate and
311 free-wing, respectively). Therefore, for further comparison, all dust sample compositions are merged and separated by sulfate
312 intrusion periods. This was done primarily because the collection efficiency by size is less relevant to the fractional contribution
313 of each mineral type per size, and therefore integrating all the techniques together improves the statistics for each size with a
314 higher number of particles analyzed.

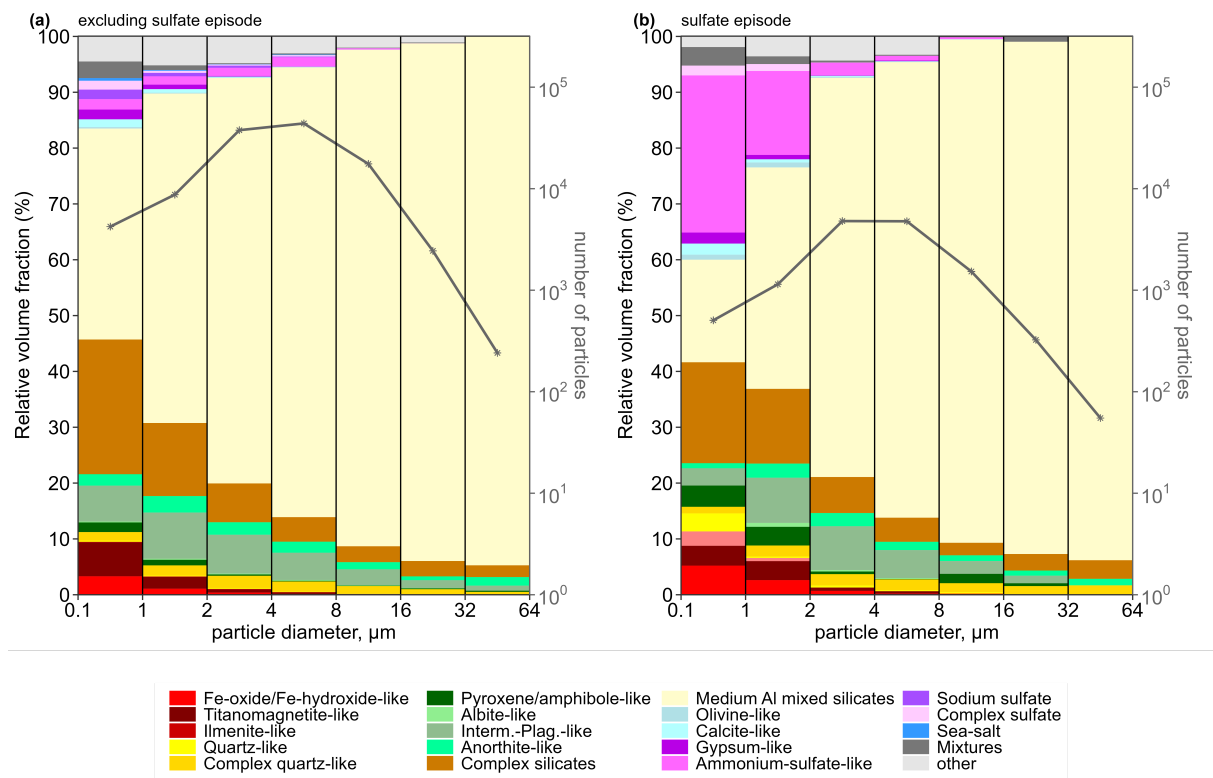


Figure 4. Size-resolved relative volume fraction of different particle groups at Dyngjúsandur, Iceland in 2021. The curve shows the number of particles analyzed for each size bin. For simplification of display, several composition groups have been combined in this plot. The "Complex silicates" class consists of the groups (Complex silicate (high Al), Complex silicate (moderat Al-low alkali), Al-rich clay mineral, Other silicate, Ca-rich silicate/Ca-Si-mixture); the "Mixtures" class comprises the groups (Sea-salt/silicate mixture, Aged sea-salt/silicate mixture, Sodium sulfate/silicate mixture, Sulfate/silicate mixture, Complex mixture). For details on the classification scheme refer to the supplement S3.

315 Excluding the sulfate episodic samples, in the 0.1–1 μm size, the dominant particle class are, by volume, MAS (38 %) and
 316 complex silicate (24 %) followed by Interm-Plag.-like (6 %), Titanomagnetite-like (4 %) and Fe-oxide/Fe-hydroxide (3 %)
 317 occurring mostly in this size interval. In addition, trace amounts of salt and sulfate mixtures were also observed. In the 1–2 μm
 318 size, the relative volume fractions of MAS, complex silicate, and Interm-Plag.-like are 59 %, 13 %, and 8 % respectively, with
 319 Fe-oxide/Fe-hydroxide at 1 %. In general, the MAS is a major composition present in all size range and displays an increasing
 320 contribution with particle size, while Fe-rich particles contributions are mostly limited to diameters below 2 μm . A decrease in
 321 relative volume fraction is also observed for Titanomagnetite-like particles (1.5 %) in this size range. From particle diameters
 322 between 2 and 8 μm 72–80 % of the particles fall under MAS with Interm-Plag.-like and complex silicates being the other
 323 two main particle types at around 6 % and 5 % respectively. The contribution of Fe-rich particles is < 0.5 % while that of
 324 Titanomagnetite-like particles is < 0.4 %. Finally, for particle sizes greater than 8 μm , more than 90 % of the particles are
 325 MAS with Fe-rich and Titanomagnetite-like particles virtually absent.

326 The major compositional variability between sampling days is due to the presence of sulfate particles. Especially the num-
 327 ber abundance of the ammonium-sulfate-like particles exhibits large differences. Ammonium sulfate particles are present in
 328 significant proportion during the periods 16 to 21 August and on 02, 03, and 05 September mainly in particles with $d_v < 4$ μm .
 329 On other days, they are almost absent or occur in minor amounts. As all of the collected particles are freshly emitted and of
 330 local origin, the observation of a high content of ammonium-sulfate particles in a few of the samples highlights the influence
 331 of volcanic emission in aerosol load as sulfur is a notable indicator of volcanic emission (Carn et al., 2009).

332 3.3 Iron distribution in Icelandic dust

333 Icelandic dust is rich in iron (Fe) (Arnalds et al., 2014) which is a key mineral affecting climatic, environmental, and biological
 334 processes (Schulz et al., 2012). Fe in Icelandic volcanic rocks (andesite and basalts) varies between 6.5 to 12.5 wt % (Jakobsson
 335 et al., 2008). For Dyngjúsandur, the reported Fe content is ~ 10 wt %, consisting primarily of volcanic glass (Baratoux et al.,
 336 2011; Baldo et al., 2020). Fe in Icelandic dust can be broadly classified into structural Fe (typically contained in pyroxene
 337 and amorphous glass) and Fe oxide-hydroxide (derived via sequential extractions) mainly magnetite (Baldo et al., 2020).
 338 Furthermore, the majority of the Fe content in Icelandic dust is attributed to structural Fe found in volcanic glass and certain
 339 iron-bearing crystalline species (González-Romero et al., 2024b). This structural Fe accounts for approximately 80 % of the
 340 total Fe content, with magnetite comprising a smaller proportion, and even less hematite and goethite (González-Romero et al.,
 341 2024b). While SEM alone cannot differentiate between free and structural Fe, by providing the total Fe content on a particle-
 342 by-particle basis, it provides a detailed Fe size distribution and some useful clues on the mixing state of Fe oxide-hydroxides.

343 To quantitatively evaluate the Fe distribution for a large number of particles, Fig. 5 shows the size-resolved abundance of
 344 "silicate" particles classified by their Fe content (ratio of Fe atomic concentration to all other major elements except H, C, N,
 345 O) in Dyngjúsandur. Here "non-silicates" are mainly sulfate- (apart from gypsum) and sea-salt-like compositions which are
 346 excluded. Four main particle types can be distinguished in the plot: (a) particles with high Fe content ($\text{IFel} > 0.5$), (b) particles
 347 with intermediate Fe content $0.1 < \text{IFel} < 0.5$, (c) particles with low Fe content ($\text{IFel} < 0.1$), and (d) particles without detectable
 348 Fe. High Fe content is mainly associated with particles of diameters less than 1 μm . In general, most particles have Fe content

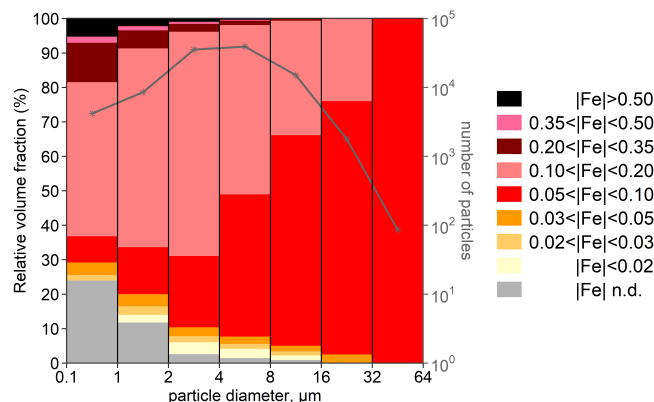


Figure 5. Size resolved iron indices for silicate particles. “n.d.” means Fe not detected.

349 between 0.05 and 0.2 which implies that Fe is either embedded in the lattice structure of the particle itself or present as small Fe
 350 (hydr)oxide accretions. Supplement S9 (g) shows an example of a Fe-rich grain attached to a MAS particle, and S8 (c) shows
 351 a Fe-Ti grain. This is also corroborated by the detailed study on the Fe mode of occurrence in sediments of Dyngjúsandur in
 352 González-Romero et al. (2024b). Fe is found in glass particles in different forms and proportions. It occurs primarily within
 353 the glass and other silicate structures. Additionally, iron can be present as exsolutions within the glass particles, resulting in
 354 the formation of magnetite, hematite, and goethite as well as nano-sized Fe oxides that are relatively more bio-accessible
 355 (González-Romero et al., 2024b).

356 Figure 6a shows the relative contribution of each particle type to Fe in every particle class. A notable contrast is evident when
 357 compared to the particle type fractions depicted in Fig. 4. Specifically, the Fe-oxide/Fe-hydroxide-like and Titanomagnetite-
 358 like particles exhibit an increased proportion due to their higher Fe content, while the fractions of sulfates, quartz, and other
 359 particle types significantly diminish, owing their lack of Fe. The Fe contribution from MAS particles follows a similar trend
 360 as observed in its size-resolved composition, indicating that these primarily glassy particles contain a substantial amount of
 361 Fe. Figure 6b provides a comparison of the mass fraction of elemental Fe as a function of particle size between Icelandic and
 362 Moroccan dust. Notably, Icelandic dust exhibits a higher total Fe content and a more pronounced decrease in Fe content with
 363 increasing particle size compared to Moroccan dust (Panta et al., 2023). Specifically, the Fe content in Icelandic dust starts at
 364 around 13 % for particles below 1 μm and gradually decreases to less than 5 % for the largest particles. In contrast, Moroccan
 365 dust displays a less pronounced reduction in Fe content with particle size, starting from approximately 8 % for particles below
 366 1 μm to around 4-5 % for particles larger than 5 μm. The gradual decrease in Fe content in Moroccan dust above 5 μm can
 367 be partly attributed to the presence of clay aggregates at large particle sizes. Conversely, Icelandic dust experience a steep
 368 reduction in fractional elemental iron with increasing particle size by a factor of up to 2.

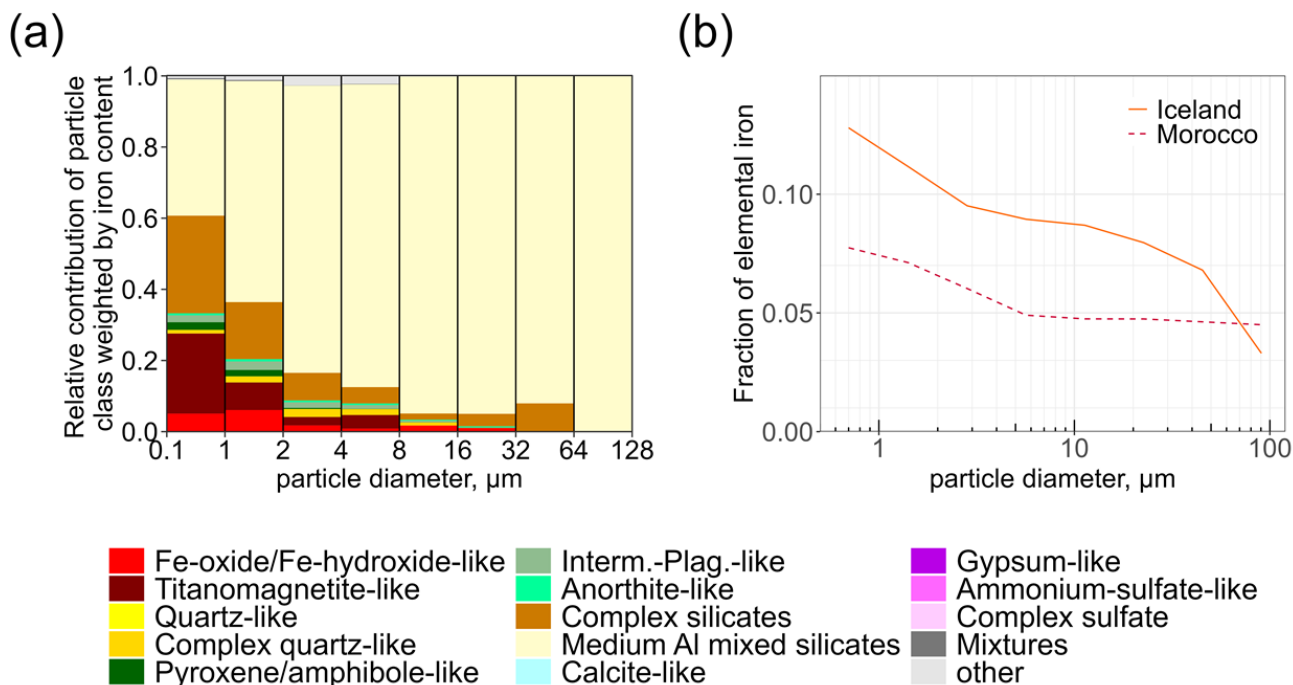


Figure 6. (a) Relative contribution of each particle class weighted by their iron content. The "Complex silicates" class consists of the groups (Complex silicate (high Al), Complex silicate (moderat Al-low alkali), Al-rich clay mineral, Other silicate, Ca-rich silicate/Ca-Si-mixture); the "Mixtures" class comprises the groups (Sea-salt/silicate mixture, Aged sea-salt/silicate mixture, Sodium sulfate/silicate mixture, Sulfate/silicate mixture, Complex mixture). For details on the classification scheme refer to the supplement S3 and (b) fraction of elemental iron by mass with respect to all the other elements. For comparison, the iron fraction from Saharan dust is also shown from Panta et al. (2023).

369 3.4 Particle shape

370 The size-resolved aspect ratio (AR) distribution, defined as the ratio of the major to minor axis of the elliptical fit, is shown
 371 in Fig. 7a and listed in Table 3. The results highlight an increase in AR with increasing particle size. The collected aerosol
 372 particles in this study had AR ranging from 1.03 to 19.65. However, the majority ($\sim 99\%$) of particles had $\text{AR} < 3$ (see also
 373 Fig. S3 in the Supplement).

374 The AR among different particle groups have median values ranging from 1.34 to 1.45 for fine dust, 1.36 to 1.50 for coarse
 375 dust, and 1.28 to 1.58 for super-coarse dust. Notably, ammonium-sulfate-like and gypsum-like particles had some extreme
 376 shapes as indicated by their high standard deviation in aspect ratio. The most abundant particle type MAS has median values
 377 ranging from 1.37 in fine dust to 1.53 for super-coarse dust. The size dependence of the median AR as well as its variability
 378 (0.1–0.9 quantiles) is shown in Fig. 7a. For comparison, the size resolved median AR for Moroccan dust (Panta et al., 2023)

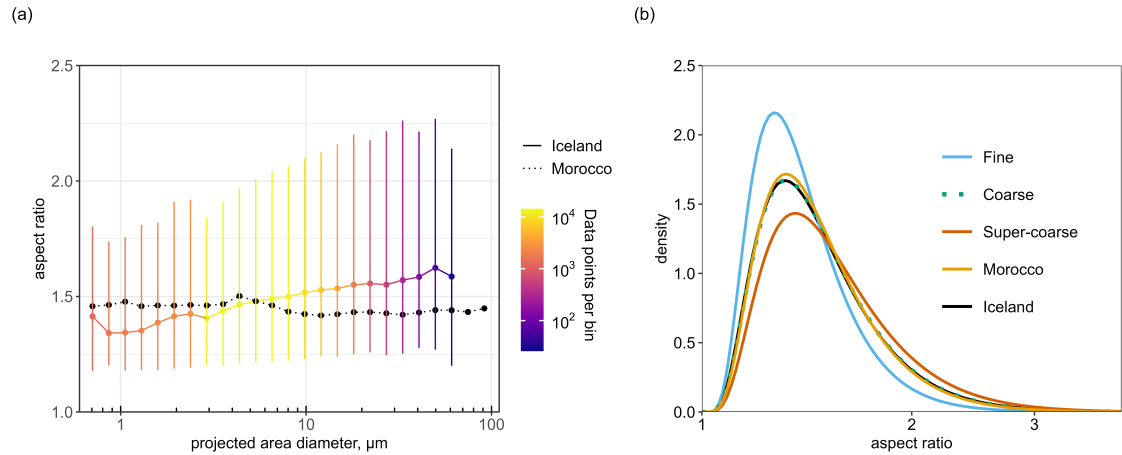


Figure 7. (a) Size-resolved particle AR. The bar range represents the range between 0.1 and 0.9 quantiles with dot being the median and the bins are color coded by the number of data points within each bin. For comparison the median AR of freshly emitted Saharan dust (Panta et al., 2023) is shown by filled black dots. (b) Parameterized aspect ratio density distributions of Icelandic dust as well as distribution for Moroccan dust (Panta et al., 2023). Furthermore, the density distribution for Icelandic dust classified as fine, coarse, and super-coarse is also shown (see section 2.3.3 for definition).

is also shown. It can be seen that for Moroccan dust, the median AR is 1.46 and is relatively constant up to 5 μm and is only slightly lower for larger particles. However, for Icelandic dust the AR consistently increases with particle size. Note that the number of particles available in size bins greater than 60 μm is low, leading to high uncertainty.

The distribution of the AR of Icelandic dust can be described by a modified log-normal function (Kandler et al., 2007) with high accuracy:

$$h(AR) = \frac{1}{\sqrt{2\pi} \cdot (AR - 1) \cdot \sigma} \times \exp \left[-\frac{1}{2} \left(\frac{\ln(AR - 1) - \mu}{\sigma} \right)^2 \right] \quad (5)$$

where σ and μ are the distribution parameters. The AR distribution is shown in Fig. 7b for different size fractions. For comparison, the distribution of dust emitted from the Moroccan Sahara (Panta et al., 2023) is also shown. The variability in AR across different particle types is generally limited, except for ammonium-sulfate-like particles, which show a broader range of AR values—particularly in the coarse and super-coarse size fractions. This increased variability likely reflects the more irregular and diverse morphologies of these particles at larger sizes. Overall, AR tends to increase with particle size across all particle types, suggesting that size has a stronger influence on particle morphology than mineralogical composition. This size-dependent trend implies that larger particles, regardless of mineral type, are more likely to exhibit elongated or irregular shapes. The AR distribution is slightly narrower in the fine size range, with a median of 1.37, whereas the coarse and super-coarse ranges show broader distributions, with medians of 1.46 and 1.53, respectively. This broader AR spread at larger sizes

Table 3. Aspect ratio mean, median and standard deviation (SD) for particle group in fine, coarse, and super-coarse dust mode. Values are not shown for size intervals with less than 40 particles.

Particle type	Fine dust ($d_p < 2.5 \mu\text{m}$)			Coarse dust ($2.5 \leq d_p < 10 \mu\text{m}$)			Super-coarse dust ($10 \leq d_p < 62.5 \mu\text{m}$)		
	Mean	Median	SD	Mean	Median	SD	Mean	Median	SD
Fe-oxide/Fe-hydroxide-like	1.41	1.34	0.27	1.55	1.46	0.39			
Titanomagnetite-like	1.39	1.34	0.28	1.43	1.39	0.22			
Quartz-like	1.52	1.39	0.38	1.56	1.45	0.34			
Complex quartz-like	1.48	1.42	0.32	1.55	1.48	0.33	1.62	1.52	0.36
Pyroxene/amphibole-like	1.44	1.35	0.27	1.57	1.49	0.33	1.64	1.55	0.38
Albite-like				1.48	1.40	0.26			
Interm.-Plag.-like	1.42	1.34	0.28	1.51	1.44	0.30	1.56	1.50	0.32
Anorthite-like	1.43	1.35	0.27	1.53	1.45	0.32	1.63	1.55	0.37
Complex silicate (moderat Al-low alkali)	1.43	1.35	0.27	1.46	1.39	0.28	1.47	1.42	0.25
Complex silicate (high Al)	1.46	1.35	0.36	1.56	1.47	0.35			
Al-rich clay mineral	1.52	1.45	0.30	1.54	1.46	0.31			
Other silicate	1.51	1.41	0.37	1.54	1.46	0.35	1.68	1.58	0.50
Ca-rich silicate/Ca-Si-mixture	1.53	1.44	0.38	1.58	1.50	0.39	1.63	1.55	0.37
Medium Al mixed silicates	1.46	1.37	0.32	1.55	1.47	0.34	1.63	1.53	0.40
Olivine-like				1.62	1.54	0.35			
Calcite-like	1.41	1.34	0.26	1.53	1.44	0.37			
Gypsum-like	1.54	1.40	0.64	1.74	1.53	0.72			
Ammonium-sulfate-like	1.45	1.34	0.39	2.06	1.36	1.82	2.61	1.28	2.99
Complex sulfate	1.57	1.42	0.42	1.47	1.38	0.35			
Sulfate/silicate mixture	1.69	1.44	0.49	1.42	1.36	0.26			
Other	1.61	1.45	0.53	1.68	1.43	0.70			
All	1.47	1.37	0.34	1.55	1.46	0.42	1.63	1.53	0.47

is mainly driven by the high variability observed in MAS particles. Despite these differences, the overall shape of the AR distribution is relatively consistent with that observed in Morocco (Panta et al., 2023).

3.5 Composition at Outflow Regions

We placed flat-plate samplers at 4 different outflow regions to gain insights into the local/regional transport of dust aerosols and understand its diverse chemical compositions (Fig. 8). The codes HRS, MRS, SRS, and VFS are given to the different outflow regions with DYS representing the main site where enhanced dust emission occurs and are shown in Fig. 1. Sampling coordinates as well as sampling dates are summarized in Table S1-5. in the Supplement. The average substrate exposure in the outflow regions was ~ 48 hours. Overall, the chemical composition of the collected aerosol particles in locations HRS, MRS, and SRS does not show a significant variability and is relatively similar to the aerosol composition at the main site. Similar to the aerosol composition at the main site, we also see episodes of sulfate intrusions at HRS (17 - 21 August), MRS (17 - 19 August), SRS (17 - 21 August), and VFS (18 -20 August).

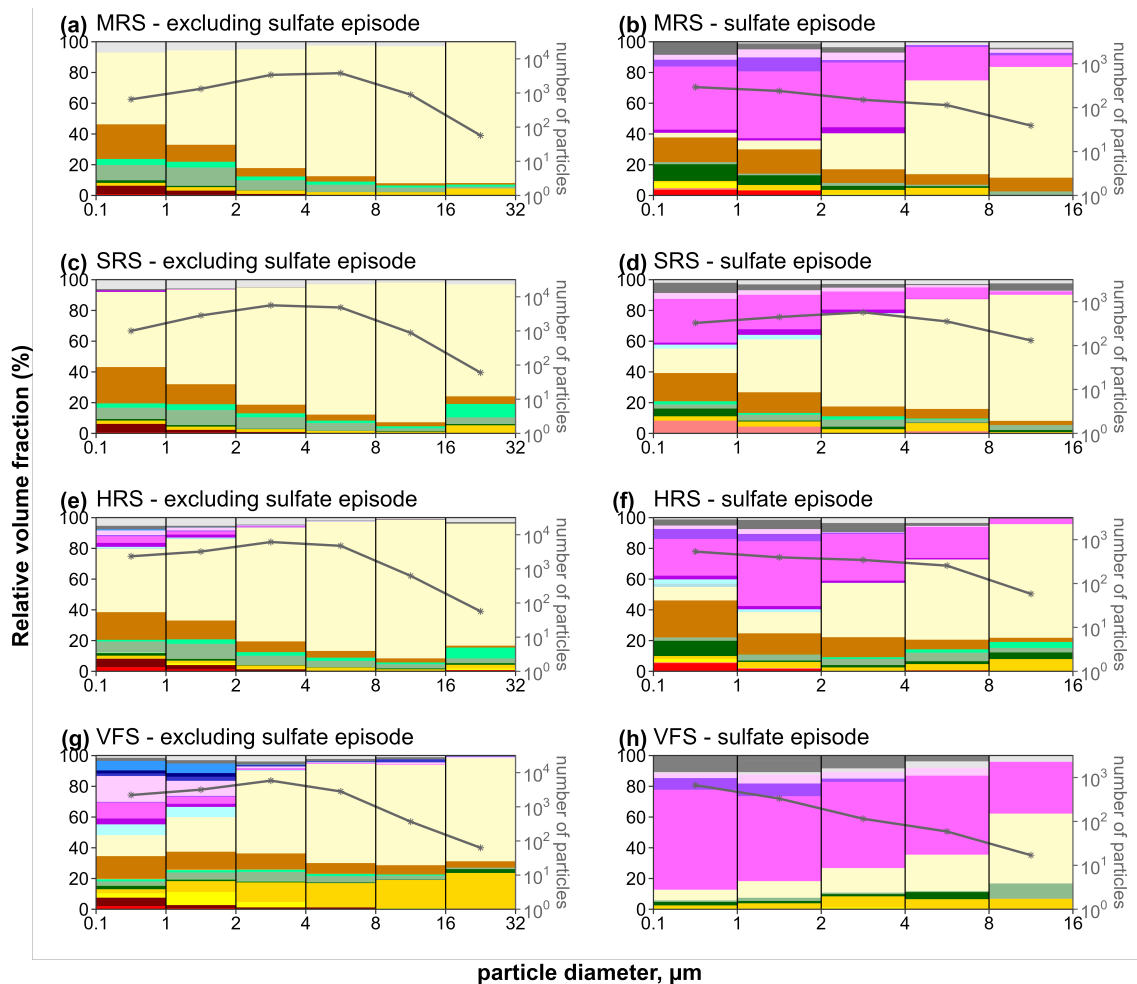


Figure 8. Size-resolved volume-averaged composition of the aerosol at different outflow regions during sulfate intrusion periods. The "Complex silicates" class consists of the groups (Complex silicate (high Al), Complex silicate (moderat Al-low alkali), Al-rich clay mineral, Other silicate, Ca-rich silicate/Ca-Si-mixture); the "Mixtures" class comprises the groups (Sea-salt/silicate mixture, Aged sea-salt/silicate mixture, Sodium sulfate/silicate mixture, Sulfate/silicate mixture, Complex mixture). For details on the classification scheme refer to the supplement S3.

405 4 Discussion

406 4.1 Aerosol composition

407 Using the elemental ratio based classification analysis from the single-particle analysis, we derived an empirical mineralogical
408 classification scheme. With the exception of few sulfate intrusion events (discussed below), aerosol composition at Dyngjusan-
409 dur was remarkably stable.

410 Around 20 % ($> 20\,000\text{ km}^2$) of Iceland are covered by volcanoclastic sandy deserts with active aeolian processes con-
411 taining sediments from both volcanic systems and eroded glaciofluvial soils (Arnalds et al., 2001, 2016). Therefore, glass, a
412 main constituent of abraded hyaloclastite, is expected as a signature compound. In hot deserts, soils undergo mineralogical
413 fractionation due to weathering and size segregation due to dust emission and transport. For instance, the emitted dust from
414 the Saharan desert typically consists of illite and kaolinite, alongside non-clay minerals including feldspar, quartz, calcite, and
415 iron oxides (Panta et al., 2023). The segregation of minerals during dust emission and transport is influenced by variations in
416 particle sizes and densities, leading heavier and larger grains to settle closer to the emission source. Conversely, mineralogical
417 fractionation is less likely in Icelandic dust due to the limited degree of weathering, which restricts the formation of minerals
418 from glassy compounds. Additionally, Icelandic dust lacks coarse and super-coarse mineral grains such as quartz, feldspar, and
419 clay aggregates (Baldo et al., 2020). This can be attributed to the relatively young geological age of Icelandic volcanic rocks,
420 which limits the extent of weathering and alteration processes, resulting in a reduced diversity of mineral compositions in the
421 emitted dust.

422 Previous analyses of Icelandic dust conducted at Dyngjúsandur (e.g. (Baratoux et al., 2011; Baldo et al., 2020)), showed that
423 the dust aerosols predominantly consist of basaltic glass. In our companion article (González-Romero et al., 2024b), a com-
424 prehensive analysis of sediments reveals that the primary components of the dust-emitting sediments in Iceland are primarily
425 composed of black volcanic glass, constituting approximately 70 to 85 % of the total weight. Following this, plagioclase and
426 pyroxenes account for approximately 10 to 15 % and 4 to 8 % respectively. Additionally, there are trace amounts of zeolites
427 and iron oxides present in small quantities (González-Romero et al., 2024b). This is consistent with the elemental data and the
428 corresponding classification obtained in this study.

429 Approximately 53% of the aerosol population in terms of number, and 65% in terms of volume, can be attributed to MAS -
430 most likely glass particles - in the fine size range. Furthermore, around 77% (number) and 82% (volume) of the particles fall into
431 the MAS category in the coarse size range, while approximately 90% (number) and 92% (volume) fall into the MAS category
432 in the super-coarse size range. Iron content analysis conducted by Baratoux et al. (2011) revealed high iron concentrations of up
433 to 10% in Dyngjúsandur, which was further confirmed by Baldo et al. (2020) with an iron content of 15%. Titanomagnetite-like
434 particles, similar to those observed in previous studies on dust and sediments (Baratoux et al., 2011; Dagsson-Waldhauserova
435 et al., 2015; Moroni et al., 2018; Baldo et al., 2020) were primarily present in the fine mode, constituting approximately 1% of
436 the volume.

437 The increase in sulfate particles observed on specific days can be attributed to the influence of volcanic emissions from
438 Fagradalsfjall. Volcanoes release various gases and aerosols during volcanic activity. These emissions often include sulfur

dioxide (SO₂) (Esse et al., 2023), which can undergo chemical reactions in the atmosphere to form sulfate particles. The sulfate enrichment occurs on 16-17 August, 19-20 August, 02-03 September, and 05 September as seen from deposition sampler and free-wing impactor measurements. The air mass provenance during sulfur enrichment periods corroborates air masses originating from the Fagradalsfjall eruption (Fig. S7 a-d in the Supplement).

Out of all four sampling sites in outflow regions, the VFS site showed the most diverse composition. As shown in Fig. 8, in the fine mode, sea-salt and calcium-rich particles along with their mixtures were present, whereas they were not observed at other sites. As sea-salt and ca-rich particles can be from the ocean, samples collected at VFS indicate the influence of transport rather than local emission. In addition, considerable amounts of complex quartz-like particles were observed in the coarse and super-coarse fractions. Nevertheless, MAS particles contributed most to the coarse and super-coarse fractions.

4.2 Iron distribution

Mineralogy of Icelandic soil surfaces of several active erosion regions including Dyngjusandur is documented to have basaltic composition (Baratoux et al., 2011; Baldo et al., 2020; González-Romero et al., 2024b). At Dyngjusandur, the sediments have an average total Fe content of 9.3 %, with the majority (79 %) existing in a structural form, while 15 % is magnetite and 5 % is composed of hematite and goethite (González-Romero et al., 2024b). Figure 5 shows the Fe distribution among the individual particles as a function of particle size. The relative fraction of Fe-rich (IFel > 0.2) particles is higher in fine mode particles, which get transported easily over long distances and could potentially influence ocean biogeochemistry.

On average, externally mixed Fe-rich particles are predominately found in size fractions below 1 micron at about 3.5 % by volume. The aspect ratio associated with these Fe-rich particles is slightly influenced by particle size (Table 3) with lower AR for fine fractions compared to coarse fractions, indicating coarse fractions are more irregular. Furthermore, Fe is detected in virtually all (> 99.9 %) of the MAS particles, which account for the highest relative fraction of particles observed by ccSEM and ~ 88 % of the total aerosol population in Dyngjusandur. This indicates that majority of the particles in Icelandic dust are associated with some level of iron content in them.

The comparison of iron distribution in particles between Icelandic and Saharan dust reveals both similarities and differences in the trends of Fe index. In both Icelandic dust and Saharan dust, most of the Fe-rich particles (IFel > 0.5) are concentrated in particles smaller than 1 µm, accounting for approximately 5% and 4% volume fraction, respectively, in that particle range, (Kandler et al., 2011, 2020; Panta et al., 2023). The relative fractions of particles for which iron is not detected show similar patterns as well. However, the in-between range exhibits significant differences. At Dyngjusandur, there is a considerably higher fraction of particles with 0.1 < IFel < 0.2, with an increase up to 4 µm and a decrease for larger diameters. On the other hand, in Morocco, this fraction decreases with increasing particle size. Similarly, the index range of 0.05 < IFel < 0.10 increases with particle size at Dyngjusandur, while it remains relatively constant in Morocco. In contrast, the higher Fe contribution to single particles at Dyngjusandur indicates a low weathering regime of Icelandic soils (Baldo et al., 2020), resulting in higher Fe content compared to Moroccan soil. This higher iron content in the emitted dust at Dyngjusandur has the potential to serve as a source of micronutrients for marine biota in the Arctic Ocean (Dagsson-Waldhauserova et al., 2013), as Fe from the glass particles is relatively mobile and therefore potentially bio-available (Baldo et al., 2020).

473 4.3 Particle shape

474 In section 3.4, we have demonstrated that Icelandic dust exhibits an increased level of asphericity with increasing size. This
475 observation aligns with the findings of Richards-Thomas et al. (2021) regarding volcanoclastic dust particles, although their
476 study utilized sphericity as a shape descriptor rather than AR. Nevertheless, the observed trend implies a similar relationship,
477 where fine particles tend to possess a more regular shape compared to coarse particles. This has potential implications for
478 the atmospheric lifetime of dust, as aspherical particles experience higher drag forces, thereby reducing their settling velocity
479 (Yang et al., 2013; Huang et al., 2020; Mallios et al., 2020). Numerous observational studies have shown the presence of coarse
480 dust particles far from their emitted source region (Weinzierl et al., 2017; van der Does et al., 2018; Varga et al., 2021) and
481 particle shape has been proposed as a contributing factor to this phenomenon. However, the understanding of the factors driving
482 the transport mechanisms remains limited. Huang et al. (2020) compared settling velocities by approximating dust particles as
483 randomly oriented tri-axial ellipsoids. Their findings suggest an approximate 20% increase in the dust's atmospheric lifetime
484 when considering non-spherical shape effects. Therefore, the enhanced asphericity observed with increasing size in Icelandic
485 dust could lead to longer atmospheric lifetime of coarse dust as approximately 10 % of these particles have AR greater than 2.

486 When comparing the particle shape obtained in this study to that of Moroccan dust (Panta et al., 2023), we observed a distinct
487 pattern: the median shape factor of Icelandic dust increases with size, while in Moroccan dust, it remains relatively constant.
488 This difference in shape behavior can be attributed to several factors related to the age and mechanical history of the parent
489 sediments.

490 In the case of Moroccan dust, the sediments are typically transported downstream from rivers and contain a high amount of
491 clay minerals, which are absent in Icelandic dust. These clay minerals have the potential to aggregate into larger soil mineral
492 grains during transport (including fluvial water cycles), resulting in particles that are already relatively rounded and exhibit a
493 lower shape factor. Additionally, lower latitude dust sediments are often relatively older in comparison to the Icelandic ones,
494 which might be as young as one day, counted from the time of glacier outflow. Therefore, the Moroccan sediments might have
495 undergone an extensive chemical weathering compared to the more mechanical processing in Iceland. Also, the rocks ground
496 down by the glacier have had probably a considerable amount of vacuoles in the size range of 50 μm and up. Breaking these into
497 pieces might yield shard-like shaped particles in the size range of several tens of microns, which on further disintegration below
498 the typical vacuole size become then less elongated. The presence of these edges suggests that the particles have undergone
499 less rounding or rounding has occurred to a lesser extent compared to low latitude dust particles.

500 Overall, the observed differences in particle shape between high latitude and mid-low latitude dust can be attributed to vari-
501 ations in the mechanical weathering processes, age of sediments, and sources of the parent materials. These factors contribute
502 to the distinct shape characteristics exhibited by dust particles.

503 4.4 Elemental vs mineralogical composition

504 Figure 9 shows the average size-resolved mineralogical and elemental composition for Icelandic and Moroccan dust respec-
505 tively. The median elemental mass ratios in our work— 3.15 (Si/Al), 1.38 (Fe/Al), and 1.41 (Fe/Ca)—are in good agreement

506 to results with the XRF analysis reported by Baldo et al. (2020) for their Dyngjusandur (D3) sample (3.26, 1.42, and 1.41,
507 respectively).

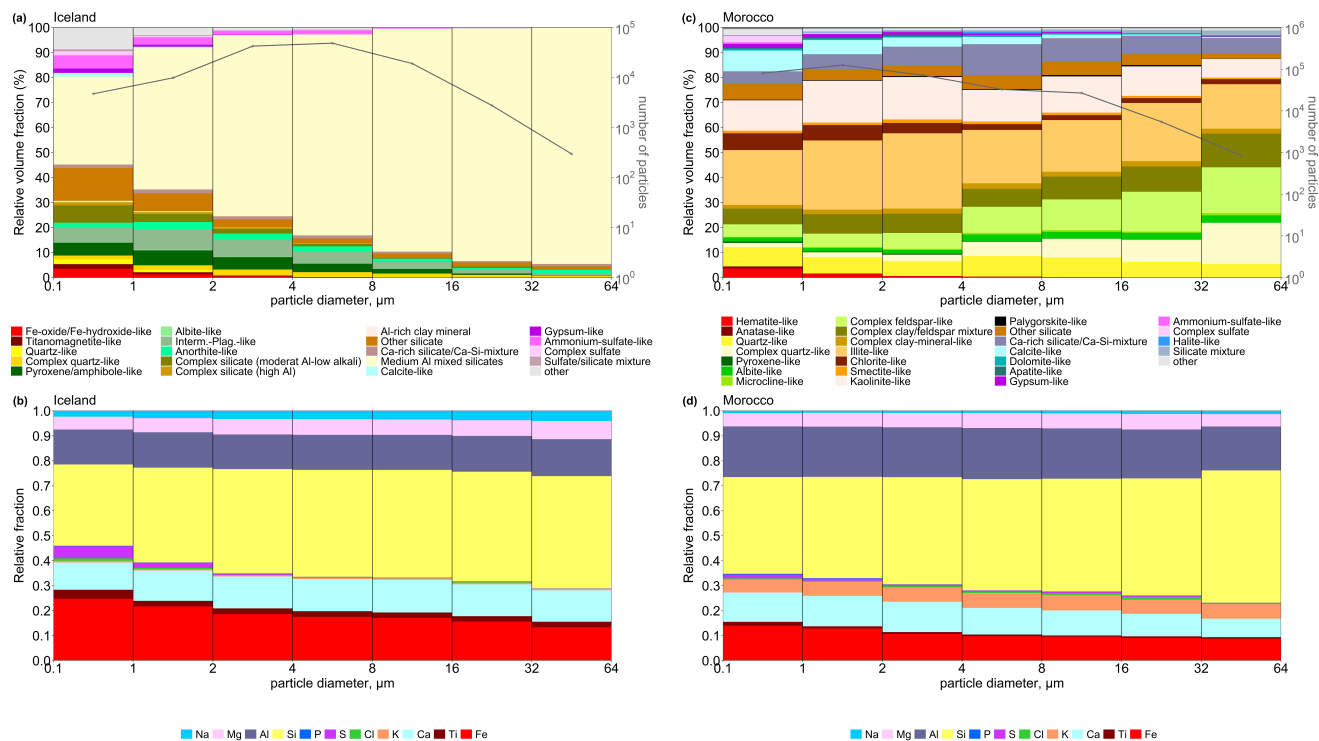


Figure 9. Size-resolved elemental and mineralogical composition for Icelandic (a,b) and Moroccan (c,d) dust, respectively.

508 When comparing particle type classifications between Icelandic and Moroccan dust, it is important to consider that the
509 identification scheme relies solely on the elemental composition of the single particles derived from EDX. Elemental compo-
510 sition alone is insufficient to accurately identify mineral phases since different mineral phases can have the same elemental
511 composition. Furthermore, the parent sediments of Icelandic and Moroccan dust differ (Baldo et al., 2020; González-Romero
512 et al., 2024b), which necessarily leads to differences in the classification scheme despite using the same rules. For example,
513 Fe-oxide/Fe-hydroxide-like in Icelandic dust is named hematite-like in Moroccan dust based on the regional mineralogical
514 composition. Comparing the elemental composition of Icelandic dust at Dyngjusandur with that of Moroccan dust at L'Bour
515 (Panta et al., 2023), Icelandic dust exhibited lower Al/Si and higher Fe/Al ratios. This difference is primarily attributed to the
516 higher iron content observed in Icelandic dust compared to northern African dust (Baldo et al., 2020). Figure 9b and 9d present
517 the bulk elemental composition of Icelandic and Moroccan dust, representing all individual particles without classification
518 into distinct groups. A notable disparity between the two is observed in the Fe fraction, where Icelandic dust exhibits an ap-
519 proximately twofold higher concentration compared to Moroccan dust. Additionally, there is a slight increase in Ca content and
520 a decrease in Al content in Icelandic dust. Moreover, K is nearly absent in Icelandic dust particles across various size classes.

521 In contrast, Ti is predominantly present in the fine fraction of Moroccan dust, particularly in approximately 18 % of silicate
522 particles. Conversely, in Icelandic dust, Ti is detected throughout the entire size range, with over 86 % of silicate particles
523 containing Ti. These findings align with the outcomes of Sanchez-Marroquin et al. (2020) study on Icelandic dust collected
524 from an aircraft, suggesting that Ti could potentially serve as a tracer for identifying Icelandic mineral dust particles.

525 However, when comparing the mineralogical composition, notable differences emerge. Icelandic dust primarily consists of
526 MAS particles, which are highly likely to be glass, intermediate plagioclase, and pyroxene. In contrast, Moroccan dust is pre-
527 dominantly composed of clays, feldspar, quartz, and calcite. These distinctions can be attributed to the differing compositions
528 of the parent sediments (Baldo et al., 2020; González-Romero et al., 2024b).

529 **5 Summary and conclusions**

530 In this paper, we determined the chemistry and morphology data of freshly emitted Icelandic dust particles identified by
531 ccSEM/EDX at Dyngjusandur and surrounding outflow locations in Iceland. We discussed the different particle types observed
532 and explored their properties.

533 Electron microscopy showed that the most abundant particle class was Medium Al mixed particles (glassy) at all of the
534 locations. Sulfate intrusion periods were observed on selected days with higher abundance of ammonium sulfate particles in
535 both the fine and coarse size range. The composition at regional outflow regions was also found to be similar to that observed
536 in Dyngjusandur except for a hill top site which had influence of transported rather than locally emitted aerosol.

537 We observed that the particles solely dominated by Fe are found mainly in fine fractions. Furthermore, a higher total Fe
538 content within individual particles is observed in Icelandic dust compared to Saharan dust which can affect the modelled dust-
539 radiation interaction as well as the supply of nutrients to terrestrial and marine ecosystems. The high Fe content in Icelandic dust
540 is associated with the composition of the parent sediments which are mainly iron-bearing glass. Baldo et al. (2020) estimated
541 Fe solubility of 0.6 % for Dyngjusandur which supplies Fe to the North Atlantic Ocean.

542 The 2-D imaging measurements revealed a systematic dependence of particle morphology on size (0.5 - 62.5 μm), consistent
543 across the entire sample set. Particle elongation, represented by aspect ratio, increased with size. Median aspect ratios for fine,
544 coarse, and super-coarse particles were 1.37, 1.46, and 1.53, respectively. Density distributions were narrower for fine mode
545 particles compared to coarse and super-coarse, indicating a wider range of aspect ratio values in the latter. These patterns in
546 aspect ratio distribution can inform parameterization of particle shape in models of dust transport, dispersion, or climate.

547 Our results highlight that on an individual particle level Icelandic and Saharan dust have relatively similar elemental compo-
548 sition, but fundamentally different mineralogy due to the different geological parent sediment. These significant compositional
549 differences have important consequences for ice nucleation, radiative forcing, and nutrient deposition. As shown in Baldo et al.
550 (2023), the complex refractive index (between 660-950 nm) of Icelandic dust from Dyngjusandur is 2-5 times higher than that
551 of Moroccan Saharan dust, likely due to its higher magnetite content. This indicates that Icelandic dust is more absorbing in
552 the near-IR band and may exert a stronger positive direct radiative effect. The exact role of black volcanic glass in dust-cloud
553 interactions is not fully understood, which hampers a comprehensive understanding of its effects on climate.

554 We observed differences in the distribution of Fe between Icelandic and Saharan dust particles, with a higher Fe contribution
555 in Icelandic dust. The overall shape distribution between Icelandic and Saharan dust is observed to be rather similar although
556 a dependency with size is observed for Icelandic dust, but not for Saharan dust.

557 Characterization of aerosol composition in highly sensitive regions such as Iceland is important for understanding the poten-
558 tial climate effects. With retreating glaciers due to increased climate warming, dust emissions are expected to increase, which
559 will likely have an impact on the Earth system in general and on the regional environment in particular. In addition to the
560 detailed characterization in this work, our measurements of the aerosol optical properties together with the PSD will provide
561 further insight into the absorption and scattering properties and PSD variability of Icelandic dust which is essential to determine
562 the radiative impact of Icelandic dust and its contribution to Arctic amplification.

563 *Data availability.* The data are publicly available in the Zenodo data repository at <https://10.5281/zenodo.15769744> (Panta et al., 2025).

564 *Author contributions.* CPG-P proposed and designed the measurement campaign with contributions from AA, PDW, SD, KK, MK, XQ,
565 and KS. AP, KK, KS, AA, PDW, SD, CGF, AGR, MK, MM, XQ, JYD, and CPGP participated in the field measurement campaign. ME
566 contributed to electron microscopy analysis. MM contributed to sample collection. AP collected the samples, analysed them by electron
567 microscopy, performed formal analysis, visualization and writing of the original draft manuscript. KK and CPG-P supervised the work.
568 CPG-P and KK re-edited the manuscript and all authors contributed in data discussion, reviewing and manuscript finalization.

569 *Competing interests.* At least one of the (co-)authors is a member of the editorial board of Atmospheric chemistry and Physics.

570 *Acknowledgements.* We acknowledge the EMIT project, which is supported by the NASA Earth Venture Instrument program, under the
571 Earth Science Division of the Science Mission Directorate. We thank Paul Ginoux for providing high-resolution global dust source maps,
572 which were very helpful for the identification of the FRAGMENT experimental sites. We thank the staff from the ranger station at Dreki
573 as well as the wardens of the Dreki campsite and the Dreki mountain rescue service for their valuable support and advice. We also thank
574 Vilhjalmur Vernharðsson and his crew from Fjalladýrð for their permanent logistic help. Without all of them, the measurement campaign
575 would not have been successfully feasible.

576 *Financial support.* The field campaign and its associated research, including this work, was funded by the European Research Council under
577 the Horizon 2020 research and innovation programme through the ERC Consolidator Grant FRAGMENT (grant agreement No. 773051) and
578 the AXA Research Fund through the AXA Chair on Sand and Dust Storms at BSC. CGF was supported by a PhD fellowship from the Agència
579 de Gestió d'Ajuts Universitaris i de Recerca (AGAUR) grant 2020_FI B 00678. KK was funded by the Deutsche Forschungsgemeinschaft

580 (DFG, German Research Foundation) – 264907654; 416816480. KS was funded by the Deutsche Forschungsgemeinschaft (DFG, German
581 Research Foundation) - 417012665. MK has received funding through the Helmholtz Association's Initiative and Networking Fund (grant
582 agreement no. VH-NG-1533). The work was partly funded by the Orkurannsóknasjóður (National Power Agency of Iceland).
583 We acknowledge support from the Open Access Publishing Fund of the Technical University of Darmstadt.

- 585 Adebisi, A., Kok, J. F., Murray, B. J., Ryder, C. L., Stuut, J.-B. W., Kahn, R. A., Knippertz, P., Formenti, P., Mahowald, N. M., Pérez García-
586 Pando, C., Klose, M., Ansmann, A., Samset, B. H., Ito, A., Balkanski, Y., Di Biagio, C., Romanias, M. N., Huang, Y., and Meng, J.: A
587 review of coarse mineral dust in the Earth system, *Aeolian Research*, 60, 100 849, <https://doi.org/10.1016/j.aeolia.2022.100849>, 2023.
- 588 Arnalds, O.: Dust sources and deposition of aeolian materials in Iceland, *Icelandic Agricultural Sciences*, pp. 3–21, 2010.
- 589 Arnalds, O., Gísladóttir, F., and Sigurjónsson, H.: Sandy deserts of Iceland: an overview, *Journal of Arid Environments*, 47, 359–371,
590 <https://doi.org/10.1006/jare.2000.0680>, 2001.
- 591 Arnalds, O., Olafsson, H., and Dagsson-Waldhauserova, P.: Quantification of iron-rich volcanogenic dust emissions and deposition over the
592 ocean from Icelandic dust sources, *Biogeosciences*, 11, 6623–6632, <https://doi.org/10.5194/bg-11-6623-2014>, 2014.
- 593 Arnalds, O., Dagsson-Waldhauserova, P., and Olafsson, H.: The Icelandic volcanic aeolian environment: Processes and impacts — A review,
594 *Aeolian Research*, 20, 176–195, <https://doi.org/10.1016/j.aeolia.2016.01.004>, 2016.
- 595 Aryal, Y. and Evans, S.: Dust emission response to precipitation and temperature anomalies under different climatic conditions, *Science of*
596 *The Total Environment*, 874, 162 335, <https://doi.org/10.1016/j.scitotenv.2023.162335>, 2023.
- 597 Baldo, C., Formenti, P., Nowak, S., Chevaillier, S., Cazaunau, M., Pangui, E., Di Biagio, C., Doussin, J.-F., Ignatyev, K., Dagsson-
598 Waldhauserova, P., Arnalds, O., MacKenzie, A. R., and Shi, Z.: Distinct chemical and mineralogical composition of Icelandic dust
599 compared to northern African and Asian dust, *Atmospheric Chemistry and Physics*, 20, 13 521–13 539, [https://doi.org/10.5194/acp-20-](https://doi.org/10.5194/acp-20-13521-2020)
600 [13521-2020](https://doi.org/10.5194/acp-20-13521-2020), 2020.
- 601 Baldo, C., Formenti, P., Di Biagio, C., Lu, G., Song, C., Cazaunau, M., Pangui, E., Doussin, J.-F., Dagsson-Waldhauserova, P., Arnalds, O.,
602 Beddows, D., MacKenzie, A. R., and Shi, Z.: Complex refractive index and single scattering albedo of Icelandic dust in the shortwave part
603 of the spectrum, *Atmospheric Chemistry and Physics*, 23, 7975–8000, <https://doi.org/10.5194/acp-23-7975-2023>, 2023.
- 604 Baratoux, D., Mangold, N., Arnalds, O., Bardintzeff, J.-M., Platevoët, B., Grégoire, M., and Pinet, P.: Volcanic sands of Iceland - Diverse
605 origins of aeolian sand deposits revealed at Dyngjúsandur and Lambahraun, *Earth Surface Processes and Landforms*, 36, 1789–1808,
606 <https://doi.org/10.1002/esp.2201>, 2011.
- 607 Björnsson, H. and Pálsson, F.: Icelandic glaciers, *Jökull*, 58, 2008.
- 608 Boulon, J., Sellegri, K., Hervo, M., and Laj, P.: Observations of nucleation of new particles in a volcanic plume, *Proceedings of the National*
609 *Academy of Sciences*, 108, 12 223–12 226, <https://doi.org/10.1073/pnas.1104923108>, 2011.
- 610 Bullard, J. E., Baddock, M., Bradwell, T., Crusius, J., Darlington, E., Gaiero, D., Gassó, S., Gísladóttir, G., Hodgkins, R., McCulloch, R.,
611 McKenna-Neuman, C., Mockford, T., Stewart, H., and Thorsteinsson, T.: High-latitude dust in the Earth system, *Reviews of Geophysics*,
612 54, 447–485, <https://doi.org/10.1002/2016RG000518>, 2016.
- 613 Butwin, M. K., Pfeffer, M. A., von Löwis, S., Støren, E. W. N., Bali, E., and Thorsteinsson, T.: Properties of dust source material and volcanic
614 ash in Iceland, *Sedimentology*, 67, 3067–3087, <https://doi.org/10.1111/sed.12734>, 2020.
- 615 Carn, S., Fioletov, V., McLinden, C., Li, C., and Krotkov, N.: A decade of global volcanic SO₂ emissions measured from space, *Scientific*
616 *Reports*, 7, <https://doi.org/10.1038/srep44095>, 2017.
- 617 Carn, S. A., Krueger, A. J., Krotkov, N. A., Yang, K., and Evans, K.: Tracking volcanic sulfur dioxide clouds for aviation hazard mitigation,
618 *Nat Hazards*, 51, 325–343, <https://doi.org/10.1007/s11069-008-9228-4>, 2009.
- 619 Claquin, T., Schulz, M., and Balkanski, Y. J.: Modeling the mineralogy of atmospheric dust sources, *Journal of Geophysical Research:*
620 *Atmospheres*, 104, 22 243–22 256, <https://doi.org/doi.org/10.1029/1999JD900416>, 1999.

621 Dagsson-Waldhauserova, P., Arnalds, O., and Olafsson, H.: Long-term frequency and characteristics of dust storm events in Northeast Iceland
622 (1949–2011), *Atmospheric Environment*, 77, 117–127, <https://doi.org/10.1016/j.atmosenv.2013.04.075>, 2013.

623 Dagsson-Waldhauserova, P., Arnalds, O., Olafsson, H., Hladil, J., Skala, R., Navratil, T., Chadimova, L., and Meinander, O.: Snow–Dust
624 Storm: Unique case study from Iceland, March 6–7, 2013, *Aeolian Research*, 16, 69–74, <https://doi.org/10.1016/j.aeolia.2014.11.001>,
625 2015.

626 Dagsson-Waldhauserova, P., Arnalds, O., and Olafsson, H.: Long-term dust aerosol production from natural sources in Iceland, *Journal of*
627 *the Air & Waste Management Association*, 67, 173–181, <https://doi.org/10.1080/10962247.2013.805703>, PMID: 28102779, 2017.

628 Deer, W. A., F., Howie, R. A., and Zussman, J.: *An Introduction to the Rock-Forming Minerals*, Mineralogical Society of Great Britain and
629 Ireland, <https://doi.org/10.1180/DHZ>, 2013.

630 Dong, Z., Brahney, J., Kang, S., Elser, J., Wei, T., Jiao, X., and Shao, Y.: Aeolian dust transport, cycle and influences in high-
631 elevation cryosphere of the Tibetan Plateau region: New evidences from alpine snow and ice, *Earth-Science Reviews*, 211, 103 408,
632 <https://doi.org/10.1016/j.earscirev.2020.103408>, 2020.

633 Dupont, S., Klose, M., Irvine, M. R., González-Flórez, C., Alastuey, A., Bonnefond, J.-M., Dagsson-Waldhauserova, P., Gonzalez-Romero,
634 A., Hussein, T., Lamaud, E., Meyer, H., Panta, A., Querol, X., Schepanski, K., Vergara Palacio, S., Wieser, A., Yus-Díez, J., Kandler, K.,
635 and Pérez García-Pando, C.: Impact of Dust Source Patchiness on the Existence of a Constant Dust Flux Layer During Aeolian Erosion
636 Events, *Journal of Geophysical Research: Atmospheres*, 129, e2023JD040 657, <https://doi.org/10.1029/2023JD040657>, 2024.

637 Esse, B., Burton, M., Hayer, C., Pfeffer, M. A., Barsotti, S., Theys, N., Barnie, T., and Titos, M.: Satellite derived SO₂ emissions
638 from the relatively low-intensity, effusive 2021 eruption of Fagradalsfjall, Iceland, *Earth and Planetary Science Letters*, 619, 118 325,
639 <https://doi.org/10.1016/j.epsl.2023.118325>, 2023.

640 Formenti, P., Schütz, L., Balkanski, Y., Desboeufs, K., Ebert, M., Kandler, K., Petzold, A., Scheuven, D., Weinbruch, S., and Zhang,
641 D.: Recent progress in understanding physical and chemical properties of African and Asian mineral dust, *Atmospheric Chemistry and*
642 *Physics*, 11, 8231–8256, <https://doi.org/10.5194/acp-11-8231-2011>, 2011.

643 Gaston, C. J.: Re-examining Dust Chemical Aging and Its Impacts on Earth’s Climate, *Accounts of Chemical Research*, 53, 1005–1013,
644 <https://doi.org/10.1021/acs.accounts.0c00102>, 2020.

645 Gonçalves Ageitos, M., Obiso, V., Miller, R. L., Jorba, O., Klose, M., Dawson, M., Balkanski, Y., Perlwitz, J., Basart, S., Di Tomaso, E.,
646 Escribano, J., Macchia, F., Montané, G., Mahowald, N. M., Green, R. O., Thompson, D. R., and Pérez García-Pando, C.: Modeling dust
647 mineralogical composition: sensitivity to soil mineralogy atlases and their expected climate impacts, *Atmospheric Chemistry and Physics*,
648 23, 8623–8657, <https://doi.org/10.5194/acp-23-8623-2023>, 2023.

649 González-Flórez, C., Klose, M., Alastuey, A., Dupont, S., Escribano, J., Etyemezian, V., Gonzalez-Romero, A., Huang, Y., Kandler, K.,
650 Nikolich, G., Panta, A., Querol, X., Reche, C., Yus-Díez, J., and Pérez García-Pando, C.: Insights into the size-resolved dust emission
651 from field measurements in the Moroccan Sahara, *Atmospheric Chemistry and Physics*, 23, 7177–7212, <https://doi.org/10.5194/acp-23-7177-2023>, 2023.

653 González-Romero, A., González-Flórez, C., Panta, A., Yus-Díez, J., Reche, C., Córdoba, P., Moreno, N., Alastuey, A., Kandler, K., Klose,
654 M., Baldo, C., Clark, R. N., Shi, Z., Querol, X., and Pérez García-Pando, C.: Variability in sediment particle size, mineralogy, and Fe
655 mode of occurrence across dust-source inland drainage basins: the case of the lower Drâa Valley, Morocco, *Atmospheric Chemistry and*
656 *Physics*, 23, 15 815–15 834, <https://doi.org/10.5194/acp-23-15815-2023>, 2023.

657 González-Romero, A., González-Flórez, C., Panta, A., Yus-Díez, J., Córdoba, P., Alastuey, A., Moreno, N., Hernández-Chiriboga, M., Kan-
658 dler, K., Klose, M., Clark, R. N., Ehlmann, B. L., Greenberger, R. N., Keebler, A. M., Brodrick, P., Green, R., Ginoux, P., Querol, X.,

and Pérez García-Pando, C.: Characterization of the particle size distribution, mineralogy, and Fe mode of occurrence of dust-emitting sediments from the Mojave Desert, California, USA, *Atmospheric Chemistry and Physics*, 24, 9155–9176, <https://doi.org/10.5194/acp-24-9155-2024>, 2024a.

González-Romero, A., González-Flórez, C., Panta, A., Yus-Díez, J., Córdoba, P., Alastuey, A., Moreno, N., Kandler, K., Klose, M., Clark, R. N., Ehlmann, B. L., Greenberger, R. N., Keebler, A. M., Brodrick, P., Green, R. O., Querol, X., and Pérez García-Pando, C.: Probing Iceland's dust-emitting sediments: particle size distribution, mineralogy, cohesion, Fe mode of occurrence, and reflectance spectra signatures, *Atmospheric Chemistry and Physics*, 24, 6883–6910, <https://doi.org/10.5194/acp-24-6883-2024>, 2024b.

Groot Zwaafink, C. D., Grythe, H., Skov, H., and Stohl, A.: Substantial contribution of northern high-latitude sources to mineral dust in the Arctic, *Journal of Geophysical Research: Atmospheres*, 121, 13,678–13,697, <https://doi.org/10.1002/2016JD025482>, 2016.

Hamilton, D. S., Perron, M. M., Bond, T. C., Bowie, A. R., Buchholz, R. R., Guieu, C., Ito, A., Maenhaut, W., Myriokefalitakis, S., Olgun, N., Rathod, S. D., Schepanski, K., Tagliabue, A., Wagner, R., and Mahowald, N. M.: Earth, Wind, Fire, and Pollution: Aerosol Nutrient Sources and Impacts on Ocean Biogeochemistry, *Annual Review of Marine Science*, 14, 303–330, <https://doi.org/10.1146/annurev-marine-031921-013612>, 2022.

Hinds, W.: *Aerosol Technology : Properties, Behavior, and Measurement of Airborne Particles*, Wiley Interscience, 1999.

Huang, Y., Kok, J. F., Kandler, K., Lindqvist, H., Nousiainen, T., Sakai, T., Adebisi, A., and Jokinen, O.: Climate Models and Remote Sensing Retrievals Neglect Substantial Desert Dust Asphericity, *Geophysical Research Letters*, 47, e2019GL086592, <https://doi.org/10.1029/2019GL086592>, 2020.

Ito, A. and Feng, Y.: Role of dust alkalinity in acid mobilization of iron, *Atmospheric Chemistry and Physics*, 10, 9237–9250, <https://doi.org/10.5194/acp-10-9237-2010>, 2010.

Jakobsson, S. P., Jónasson, K., and Sigurdsson, I. A.: The three igneous rock series of Iceland, *Jökull*, 58, 117–138, <https://doi.org/10.33799/jokull2008.58.117>, 2008.

Journet, E., Balkanski, Y., and Harrison, S. P.: A new data set of soil mineralogy for dust-cycle modeling, *Atmospheric Chemistry and Physics*, 14, 3801–3816, <https://doi.org/10.5194/acp-14-3801-2014>, 2014.

Kandler, K., Benker, N., Bundke, U., Cuevas, E., Ebert, M., Knippertz, P., Rodríguez, S., Schütz, L., and Weinbruch, S.: Chemical composition and complex refractive index of Saharan Mineral Dust at Izaña, Tenerife (Spain) derived by electron microscopy, *Atmospheric Environment*, 41, 8058–8074, <https://doi.org/10.1016/j.atmosenv.2007.06.047>, 2007.

Kandler, K., Lieke, K., Benker, N., Emmel, C., Küpper, M., Müller-Ebert, D., Ebert, M., Scheuven, D., Schladitz, A., Schütz, L., and Weinbruch, S.: Electron microscopy of particles collected at Praia, Cape Verde, during the Saharan Mineral Dust Experiment: particle chemistry, shape, mixing state and complex refractive index, *Tellus B: Chemical and Physical Meteorology*, 63, 475–496, <https://doi.org/10.1111/j.1600-0889.2011.00550.x>, 2011.

Kandler, K., Schneiders, K., Ebert, M., Hartmann, M., Weinbruch, S., Prass, M., and Pöhlker, C.: Composition and mixing state of atmospheric aerosols determined by electron microscopy: method development and application to aged Saharan dust deposition in the Caribbean boundary layer, *Atmospheric Chemistry and Physics*, 18, 13 429–13 455, <https://doi.org/10.5194/acp-18-13429-2018>, 2018.

Kandler, K., Schneiders, K., Heuser, J., Waza, A., Aryasree, S., Althausen, D., Hofer, J., Abdullaev, S. F., and Makhmudov, A. N.: Differences and Similarities of Central Asian, African, and Arctic Dust Composition from a Single Particle Perspective, *Atmosphere*, 11, <https://doi.org/10.3390/atmos11030269>, 2020.

Kawai, K., Matsui, H., and Tobo, Y.: Dominant Role of Arctic Dust With High Ice Nucleating Ability in the Arctic Lower Troposphere, *Geophysical Research Letters*, 50, e2022GL102470, <https://doi.org/10.1029/2022GL102470>, 2023.

697 Kok, J. F., Adebisi, A. A., Albani, S., Balkanski, Y., Checa-Garcia, R., Chin, M., Colarco, P. R., Hamilton, D. S., Huang, Y., Ito, A., Klose, M.,
698 Li, L., Mahowald, N. M., Miller, R. L., Obiso, V., Pérez García-Pando, C., Rocha-Lima, A., and Wan, J. S.: Contribution of the world's main
699 dust source regions to the global cycle of desert dust, *Atmospheric Chemistry and Physics*, 21, 8169–8193, [https://doi.org/10.5194/acp-](https://doi.org/10.5194/acp-21-8169-2021)
700 21-8169-2021, 2021.

701 Kok, J. F., Storelvmo, T., Karydis, V. A., Adebisi, A. A., Mahowald, N. M., Evan, A. T., He, C., and Leung, D. M.: Mineral dust aerosol
702 impacts on global climate and climate change, *Nature Reviews Earth & Environment*, 4, 71–86, [https://doi.org/10.1038/s43017-022-](https://doi.org/10.1038/s43017-022-00379-5)
703 00379-5, 2023.

704 Lamotte, C., Guth, J., Maréchal, V., Cussac, M., Hamer, P. D., Theys, N., and Schneider, P.: Modeling study of the impact of SO₂ volcanic
705 passive emissions on the tropospheric sulfur budget, *Atmospheric Chemistry and Physics*, 21, 11 379–11 404, [https://doi.org/10.5194/acp-](https://doi.org/10.5194/acp-21-11379-2021)
706 21-11379-2021, 2021.

707 Lasne, J., Urupina, D., Maters, E. C., Delmelle, P., Romanias, M. N., and Thevenet, F.: Photo-enhanced uptake of SO₂ on Icelandic volcanic
708 dusts, *Environ. Sci.: Atmos.*, 2, 375–387, <https://doi.org/10.1039/D1EA00094B>, 2022.

709 Li, W., Shao, L., Shi, Z., Chen, J., Yang, L., Yuan, Q., Yan, C., Zhang, X., Wang, Y., Sun, J., Zhang, Y., Shen, X., Wang, Z., and Wang, W.:
710 Mixing state and hygroscopicity of dust and haze particles before leaving Asian continent, *Journal of Geophysical Research: Atmospheres*,
711 119, 1044–1059, <https://doi.org/10.1002/2013JD021003>, 2014.

712 Li, W., Shao, L., Zhang, D., Ro, C.-U., Hu, M., Bi, X., Geng, H., Matsuki, A., Niu, H., and Chen, J.: A review of single aerosol particle
713 studies in the atmosphere of East Asia: morphology, mixing state, source, and heterogeneous reactions, *Journal of Cleaner Production*,
714 112, 1330–1349, <https://doi.org/10.1016/j.jclepro.2015.04.050>, preventing Smog Crises, 2016.

715 Lindqvist, H., Jokinen, O., Kandler, K., Scheuven, D., and Nousiainen, T.: Single scattering by realistic, inhomogeneous mineral dust par-
716 ticles with stereogrammetric shapes, *Atmospheric Chemistry and Physics*, 14, 143–157, <https://doi.org/10.5194/acp-14-143-2014>, 2014.

717 Mahowald, N., Albani, S., Kok, J. F., Engelstaeder, S., Scanza, R., Ward, D. S., and Flanner, M. G.: The size distribution of desert dust
718 aerosols and its impact on the Earth system, *Aeolian Research*, 15, 53–71, <https://doi.org/10.1016/j.aeolia.2013.09.002>, 2014.

719 Mallios, S. A., Drakaki, E., and Amiridis, V.: Effects of dust particle sphericity and orientation on their gravitational settling in the earth's
720 atmosphere, *Journal of Aerosol Science*, 150, 105 634, <https://doi.org/10.1016/j.jaerosci.2020.105634>, 2020.

721 Maters, E. C., Dingwell, D. B., Cimarelli, C., Müller, D., Whale, T. F., and Murray, B. J.: The importance of crystalline phases in ice
722 nucleation by volcanic ash, *Atmospheric Chemistry and Physics*, 19, 5451–5465, <https://doi.org/10.5194/acp-19-5451-2019>, 2019.

723 Meinander, O., Dagsson-Waldhauserova, P., and Arnalds, O.: Icelandic volcanic dust can have a significant influence on the cryosphere in
724 Greenland and elsewhere, *Polar Research*, 35, <https://doi.org/10.3402/polar.v35.31313>, 2016.

725 Meinander, O., Dagsson-Waldhauserova, P., Amosov, P., Aseyeva, E., Atkins, C., Baklanov, A., Baldo, C., Barr, S. L., Barzycka, B., Ben-
726 ning, L. G., Cvetkovic, B., Enchilik, P., Frolov, D., Gassó, S., Kandler, K., Kasimov, N., Kavan, J., King, J., Koroleva, T., Krupskaya,
727 V., Kulmala, M., Kusiak, M., Lappalainen, H. K., Laska, M., Lasne, J., Lewandowski, M., Luks, B., McQuaid, J. B., Moroni, B., Mur-
728 ray, B., Möhler, O., Nawrot, A., Nickovic, S., O'Neill, N. T., Pejanovic, G., Popovicheva, O., Ranjbar, K., Romanias, M., Samonova,
729 O., Sanchez-Marroquin, A., Schepanski, K., Semenov, I., Sharapova, A., Shevnina, E., Shi, Z., Sofiev, M., Thevenet, F., Thorsteins-
730 son, T., Timofeev, M., Umo, N. S., Uppstu, A., Urupina, D., Varga, G., Werner, T., Arnalds, O., and Vukovic Vimic, A.: Newly iden-
731 tified climatically and environmentally significant high-latitude dust sources, *Atmospheric Chemistry and Physics*, 22, 11 889–11 930,
732 <https://doi.org/10.5194/acp-22-11889-2022>, 2022.

733 Moroni, B., Arnalds, O., Dagsson-Waldhauserová, P., Crocchianti, S., Vivani, R., and Cappelletti, D.: Mineralogical and Chemical Records
 734 of Icelandic Dust Sources Upon Ny-Ålesund (Svalbard Islands), *Frontiers in Earth Science*, 6, <https://doi.org/10.3389/feart.2018.00187>,
 735 2018.

736 Murray, B. J., Carslaw, K. S., and Field, P. R.: Opinion: Cloud-phase climate feedback and the importance of ice-nucleating particles,
 737 *Atmospheric Chemistry and Physics*, 21, 665–679, <https://doi.org/10.5194/acp-21-665-2021>, 2021.

738 Nousiainen, T. and Kandler, K.: Light scattering by atmospheric mineral dust particles, pp. 3–52, Springer Berlin Heidelberg, Berlin, Hei-
 739 delberg, https://doi.org/10.1007/978-3-642-37985-7_1, 2015.

740 Ott, D. K. and Peters, T. M.: A Shelter to Protect a Passive Sampler for Coarse Particulate Matter, PM10 - 2.5, *Aerosol Science and*
 741 *Technology*, 42, 299–309, <https://doi.org/10.1080/02786820802054236>, 2008.

742 Panta, A., Kandler, K., Alastuey, A., González-Flórez, C., González-Romero, A., Klose, M., Querol, X., Reche, C., Yus-Díez, J., and
 743 Pérez García-Pando, C.: Insights into the single-particle composition, size, mixing state, and aspect ratio of freshly emitted mineral
 744 dust from field measurements in the Moroccan Sahara using electron microscopy, *Atmospheric Chemistry and Physics*, 23, 3861–3885,
 745 <https://doi.org/10.5194/acp-23-3861-2023>, 2023.

746 Panta, A., Kandler, K., Schepanski, K., Alastuey, A., Waldhauserova, P. D., Dupont, S., Eknayan, M., González-Flórez, C., González-Romero,
 747 A., Klose, M., Montag, M., Querol, X., Yus-Díez, J., and García-Pando, C. P.: Unveiling single-particle composition, size, shape, and mix-
 748 ing state of freshly emitted Icelandic dust via electron microscopy analysis, Zenodo [data set], <https://doi.org/10.5281/zenodo.15769744>,
 749 2025.

750 Paramonov, M., David, R. O., Kretzschmar, R., and Kanji, Z. A.: A laboratory investigation of the ice nucleation efficiency of three types of
 751 mineral and soil dust, *Atmospheric Chemistry and Physics*, 18, 16 515–16 536, <https://doi.org/10.5194/acp-18-16515-2018>, 2018.

752 Perlwitz, J. P., Pérez García-Pando, C., and Miller, R. L.: Predicting the mineral composition of dust aerosols – Part 2: Model evaluation and
 753 identification of key processes with observations, *Atmospheric Chemistry and Physics*, 15, 11 629–11 652, [https://doi.org/10.5194/acp-](https://doi.org/10.5194/acp-15-11629-2015)
 754 [15-11629-2015](https://doi.org/10.5194/acp-15-11629-2015), 2015.

755 Prospero, J. M., Bullard, J. E., and Hodgkins, R.: High-Latitude Dust Over the North Atlantic: Inputs from Icelandic Proglacial Dust Storms,
 756 *Science*, 335, 1078–1082, <https://doi.org/10.1126/science.1217447>, 2012.

757 Richards-Thomas, T., McKenna-Neuman, C., and Power, I. M.: Particle-scale characterization of volcanoclastic dust sources within Iceland,
 758 *Sedimentology*, 68, 1137–1158, <https://doi.org/10.1111/sed.12821>, 2021.

759 Sanchez-Marroquin, A., Arnalds, O., Baustian-Dorsi, K. J., Browse, J., Dagsson-Waldhauserova, P., Harrison, A. D., Maters, E. C., Pringle,
 760 K. J., Vergara-Temprado, J., Burke, I. T., McQuaid, J. B., Carslaw, K. S., and Murray, B. J.: Iceland is an episodic source of atmospheric
 761 ice-nucleating particles relevant for mixed-phase clouds, *Science Advances*, 6, eaba8137, <https://doi.org/10.1126/sciadv.aba8137>, 2020.

762 Scheuven, D., Kandler, K., Küpper, M., Lieke, K., Zorn, R., Ebert, M., Schütz, L., and Weinbruch, S.: Individual-particle analysis of
 763 airborne dust samples collected over Morocco in 2006 during SAMUM 1, *Tellus B: Chemical and Physical Meteorology*, 63, 512–530,
 764 <https://doi.org/10.1111/j.1600-0889.2011.00554.x>, 2011.

765 Schmale, J., Zieger, P., and Ekman, A. M.: Aerosols in current and future Arctic climate, *Nature Climate Change*, 11, 95–105,
 766 <https://doi.org/10.1038/s41558-020-00969-5>, 2021.

767 Schulz, M., Prospero, J. M., Baker, A. R., Dentener, F., Ickes, L., Liss, P. S., Mahowald, N. M., Nickovic, S., García-Pando, C. P., Rodríguez,
 768 S., Sarin, M., Tegen, I., and Duce, R. A.: Atmospheric Transport and Deposition of Mineral Dust to the Ocean: Implications for Research
 769 Needs, *Environmental Science & Technology*, 46, 10 390–10 404, <https://doi.org/10.1021/es300073u>, 2012.

770 Shi, Y., Liu, X., Wu, M., Zhao, X., Ke, Z., and Brown, H.: Relative importance of high-latitude local and long-range-transported dust
771 for Arctic ice-nucleating particles and impacts on Arctic mixed-phase clouds, *Atmospheric Chemistry and Physics*, 22, 2909–2935,
772 <https://doi.org/10.5194/acp-22-2909-2022>, 2022.

773 Shi, Z., Krom, M. D., Jickells, T. D., Bonneville, S., Carslaw, K. S., Mihalopoulos, N., Baker, A. R., and Benning, L. G.: Impacts
774 on iron solubility in the mineral dust by processes in the source region and the atmosphere: A review, *Aeolian Research*, 5, 21–42,
775 <https://doi.org/10.1016/j.aeolia.2012.03.001>, 2012.

776 Sokolik, I. N., Toon, O. B., and Bergstrom, R. W.: Modeling the radiative characteristics of airborne mineral aerosols at infrared wavelengths,
777 *Journal of Geophysical Research: Atmospheres*, 103, 8813–8826, <https://doi.org/10.1029/98JD00049>, 1998.

778 Song, Q., Ginoux, P., Gonçalves Ageitos, M., Miller, R. L., Obiso, V., and Pérez García-Pando, C.: Modeling impacts of dust mineralogy on
779 fast climate response, *Atmospheric Chemistry and Physics*, 24, 7421–7446, <https://doi.org/10.5194/acp-24-7421-2024>, 2024.

780 Urupina, D., Lasne, J., Romanias, M., Thiery, V., Dagsson-Waldhauserova, P., and Thevenet, F.: Uptake and surface chemistry of SO₂ on
781 natural volcanic dusts, *Atmospheric Environment*, 217, 116 942, <https://doi.org/10.1016/j.atmosenv.2019.116942>, 2019.

782 van der Does, M., Knippertz, P., Zschenderlein, P., Harrison, R. G., and Stuut, J.-B. W.: The mysterious long-range transport of giant mineral
783 dust particles, *Science Advances*, 4, eaau2768, <https://doi.org/10.1126/sciadv.aau2768>, 2018.

784 Varga, G., Dagsson-Waldhauserová, P., Gresina, F., and Helgadóttir, A.: Saharan dust and giant quartz particle transport towards Iceland,
785 *Scientific reports*, 11, 1–12, <https://doi.org/10.1038/s41598-021-91481-z>, 2021.

786 Vogel, A., Diplas, S., Durant, A. J., Azar, A. S., Sunding, M. F., Rose, W. I., Sytchkova, A., Bonadonna, C., Krüger, K., and Stohl, A.:
787 Reference data set of volcanic ash physicochemical and optical properties, *Journal of Geophysical Research: Atmospheres*, 122, 9485–
788 9514, <https://doi.org/10.1002/2016JD026328>, 2017.

789 Waldhauserova, P., Arnalds, O., Ólafsson, H., Skrabalova, L., Sigurðardóttir, G., Branis, M., Hladil, J., Skala, R., Navratil, T., Chadimova, L.,
790 Löwis, S., Thorsteinsson, T., Carlsen, H., and Jónsdóttir, I.: Physical properties of suspended dust during moist and low wind conditions
791 in Iceland, *Iceland. Agr. Sci.*, 27, 25–39, 2014.

792 Waza, A., Schneiders, K., May, J., Rodríguez, S., Eppler, B., and Kandler, K.: Field comparison of dry deposition samplers for collec-
793 tion of atmospheric mineral dust: results from single-particle characterization, *Atmospheric Measurement Techniques*, 12, 6647–6665,
794 <https://doi.org/10.5194/amt-12-6647-2019>, 2019.

795 Weinzierl, B., Ansmann, A., Prospero, J. M., Althausen, D., Benker, N., Chouza, F., Dollner, M., Farrell, D., Fomba, W. K., Freudenthaler,
796 V., Gasteiger, J., Groß, S., Haarig, M., Heinold, B., Kandler, K., Kristensen, T. B., Mayol-Bracero, O. L., Müller, T., Reitebuch, O., Sauer,
797 D., Schäfler, A., Schepanski, K., Spanu, A., Tegen, I., Toledano, C., and Walser, A.: The Saharan Aerosol Long-Range Transport and
798 Aerosol–Cloud-Interaction Experiment: Overview and Selected Highlights, *Bulletin of the American Meteorological Society*, 98, 1427 –
799 1451, <https://doi.org/10.1175/BAMS-D-15-00142.1>, 2017.

800 Wittmann, M., Groot Zwaafink, C. D., Steffensen Schmidt, L., Guðmundsson, S., Pálsson, F., Arnalds, O., Björnsson, H., Thorsteins-
801 son, T., and Stohl, A.: Impact of dust deposition on the albedo of Vatnajökull ice cap, Iceland, *The Cryosphere*, 11, 741–754,
802 <https://doi.org/10.5194/tc-11-741-2017>, 2017.

803 Xi, Y., Xu, C., Downey, A., Stevens, R., Bachelder, J. O., King, J., Hayes, P. L., and Bertram, A. K.: Ice nucleating properties of airborne dust
804 from an actively retreating glacier in Yukon, Canada, *Environ. Sci.: Atmos.*, 2, 714–726, <https://doi.org/10.1039/D1EA00101A>, 2022.

805 Yang, W., Marshak, A., Kostinski, A. B., and Várnai, T.: Shape-induced gravitational sorting of Saharan dust during transatlantic voyage: Evi-
806 dence from CALIOP lidar depolarization measurements, *Geophysical Research Letters*, 40, 3281–3286, <https://doi.org/10.1002/grl.50603>,
807 2013.

808 Yoshida, A., Moteki, N., Ohata, S., Mori, T., Tada, R., Dagsson-Waldhauserová, P., and Kondo, Y.: Detection of light-
809 absorbing iron oxide particles using a modified single-particle soot photometer, *Aerosol Science and Technology*, 50, 1–4,
810 <https://doi.org/10.1080/02786826.2016.1146402>, 2016.